Physical and mechanical controls of matrix permeability on rocks from Rotokawa Geothermal Field, Taupo Volcanic Zone, New Zealand

A thesis submitted in partial fulfilment of the requirements for the degree of

Master of Science in Engineering Geology

at the

University of Canterbury

by

Timothy Peter Carey Jones

Department of Geological Sciences
University of Canterbury
Christchurch, New Zealand
2016

Abstract

The Taupo Volcanic Zone (TVZ), situated in the central North Island of New Zealand, is the host of an active volcanic region with an enormous heat flux (4200±500 MW). Twenty-three geothermal fields lie within TVZ, seven of which have been developed for geothermal power generation, including the Rotokawa Geothermal Field (RGF), where 3% of New Zealand's power is generated.

Relationships between key mechanical properties, such as porosity and permeability, can be complex. Developing an understanding of such relationships in the subsurface helps with the optimisation and maintenance of geothermal resources.

In this thesis, a systematic physical and mechanical property study was carried out in laboratory conditions on rocks from the RGF, including rhyolite, ignimbrite, andesite and basement greywacke. Physical properties investigated were porosity, density, matrix permeability, ultrasonic wave velocities, triaxial strength and microstructure analysis.

It was determined that there is a distinct relationship between increasing porosity and increasing permeability represented by a single power-law function. However, the contrast between two andesite samples highlights how complex this relationship is. The two samples have similar porosities, yet due to differing microstructure, permeabilities are nearly two orders of magnitude different. The behaviour during triaxial testing was also significantly different between these samples, where the presence of pre-existing microfractures in one resulted in more brittle behaviour than the other.

Increasing confining stress decreases matrix permeability for the majority of samples. The decrease in permeability is more pronounced for samples with pre-existing microfractures, compared to those with no microfractures. Relationships between ultrasonic wave velocities and other parameters are weak. There is no distinct relationship between in situ permeability and depth.

The significance of microstructure and the variability in the mechanical relationships described in this thesis demonstrate the importance of thorough investigation of localised samples, especially when hosted in a hydrothermally active system.

Acknowledgements

Dr Marlène Villeneuve, Dr Paul Siratovich and Prof. Jim Cole, thank you for the time you all have given me and my project. Marlène, thank you for all your help deciphering my data and helping me construct my thesis. Your knowledge was invaluable and thanks for keeping me enthused with the project, even when things were challenging. Paul, your help with the permeameter was much appreciated, especially when equipment wasn't operating quite as it should. Jim, thank you for all your proof reading, mentoring and enthusiasm towards my project.

Thank you to Mighty River Power for giving me the opportunity to take part in this project, organising a Callaghan Scholarship and providing me with rocks to play with. Steve Sewell, thank you for showing me around Rotokawa Geothermal Field and your insight during my project, good luck for the beginning of your PhD this year.

To all the technical team on first floor; Cathy, Sarah, Rob, Chris, Matt, Sacha and Kerry, thank you for all your help in the labs, especially with fixing equipment that decided to have a break.

To the crew in room 401, especially Georgie and Michael, thanks for keeping me sane with good chat and providing discussion. Cheers Michael for helping out with the lab work, good luck for your last couple of months on your thesis!

And finally, thank you to my friends and family, in particular Mum, Dad, Josh and my flatmates, for supporting me along the way, and thanks for putting up with me in the final month where I wasn't quite as much fun as usual!

Contents

List of Figures

List of Tables

Chapter 1

Introduction

1.1 Geothermal Systems

Geothermal systems are areas where ground water comes into contact with thermal energy (largely associated with magmatic activity from the Earth's mantle), resulting in complex geological networks of heated water and altered rocks in both subsurface and surface environments (Bowen, 1979).

Geothermal systems have been exploited worldwide for the last 2000 years, for cultural purposes and mineral extraction (Grant and Bixley, 2011), but it was not until 1856 that exploratory drilling was first carried out for power generation in Lardello, Italy, with the first power generated almost 50 years later in 1904 (Cataldi et al., 1999). Since then, geothermal resources have been explored, developed and successfully exploited for power generation throughout the world, including New Zealand.

In New Zealand the main geothermal activity is in the Taupo Volcanic Zone (TVZ), a very active volcanic region with a remarkable heat flux (4200±500 MW; Hochstein 1995; Bibby et al. 1995). TVZ has successfully been utilised for power generation over the last 57 years, starting with the Wairakei Power Station, which was commissioned in 1958 (Lind et al., 2015). There are currently seven fields which have been commercially developed for power generation in the TVZ, including the Rotokawa Geothermal Field (RGF), which is the study area of this thesis.

Currently, 16% of New Zealand's total electricity is generated from geothermal power, classing it as a primary energy resource (MBIE, 2015). Geothermal systems supply reliable and renewable base load electricity and are particularly valuable in times of drought where hydroelectric dams feeding the power stations are low (O'Brien, 2010).

The scale of geothermal energy in New Zealand highlights the importance of researching these active fields, ensuring they operate efficiently and are effectively maintained to

continue to generate power into the future.

There are three factors controlling whether a geothermal resource is viable for power generation; a heat source, source of ground water and a fracture network (Bowen, 1979). The heat provides initial energy, the ground water provides a mode of transport for this energy and the fracture network allows a pathway for this heated fluid to flow, ultimately to the surface (Grant and Bixley, 2011).

The nature of fractures, at all scales, are important to understand as they dominate the fluid flow in geothermal systems. The physical and mechanical properties of the rocks hosting fracture networks (such as permeability, porosity and density) vary significantly due to variable heat fluxes, dynamic fluid flow regimes and active tectonics which are present in geothermal systems. This produces a field of highly altered, fractured and micro-structurally complex rocks (Siratovich et al., 2014).

Investigating relationships between key mechanical properties can be complicated, but developing an understanding and attempting to quantify such relationships in the subsurface can help facilitate the optimisation and maintenance of geothermal resources (e.g. Grant and Bixley, 2011; Siratovich et al., 2014).

1.1.1 Taupo Volcanic Zone

The Taupo Volcanic Zone (TVZ) has developed over the last ∼2 Ma, and has become one of the most active regions of silicic volcanism in the world (Houghton et al., 1995). It is related to the active rifting arc/back-arc system, associated with the Hikurangi subduction trough where the Pacific Plate descends underneath the Australia plate (Figure 1.1; Cole et al., 2014).

The eastern part of the North Island is rotating clockwise at 0.5–3.8° Myr^{-1} relative to the Australia plate (Wallace, 2004). Rifting within the TVZ is largely caused by roll-back because of the clockwise rotation (Wallace, 2004).

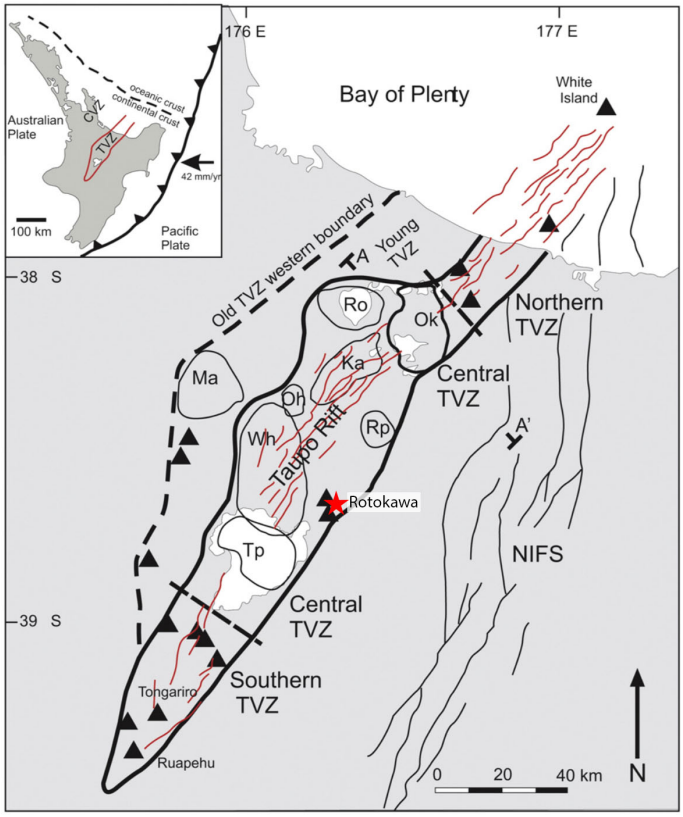

Figure 1.1: Regional map showing the location of the Taupo Volcanic Zone (TVZ) and its associated tectonic and volcanic structures (after Deering et al. 2011). The outline of Old TVZ and Young TVZ, and division into Northern TVZ, Central TVZ and Southern TVZ are from Wilson et al. (1995). Mapped faults in the Taupo Rift are from Gravley et al. (2007); Calderas are as follows: Ma = Mangakino; Ka = Kapenga; Wh = Whakamaru; Ro = Rotorua; Rp = Reporoa; Oh = Ohakuri; Tp = Taupo; Ok = Okataina (Okataina Volcanic Centre; with heavier outline). Black triangles show sites of andesite cones. NIFS = North Island Fault System. Inset shows the location of TVZ and the Coromandel Volcanic Zone (CVZ) within the North Island of New Zealand and their relationship to subduction of the Pacific plate beneath the Australian plate. Location of Rotokawa is highlighted by the red star. Original figure and caption from Cole et al. (2014)

TVZ is up to 60 km at the widest point and approximately 300 km long and is typically divided into three zones; northern, southern and central. The northern and southern zones are characterised by andesitic to dacitic volcanoes while in the central zone is dominated by rhyolite/basalt volcanoes and calderas (Wilson et al., 1995;

Houghton et al., 1995). The thickness of crust beneath TVZ is estimated to be <15 km. The basement of this is largely greywacke with volcaniclastic rocks occupying the upper 4-5 km (Cole et al., 2014).

There are 23 geothermal systems, including 17 high temperature systems (>250° C) within the greater TVZ area (Bibby et al., 1995) (Figure 1.2). The crustal heat transfer is very intense on a world scale, similar to that of Yellowstone National Park, USA (Giggenbach, 1995).

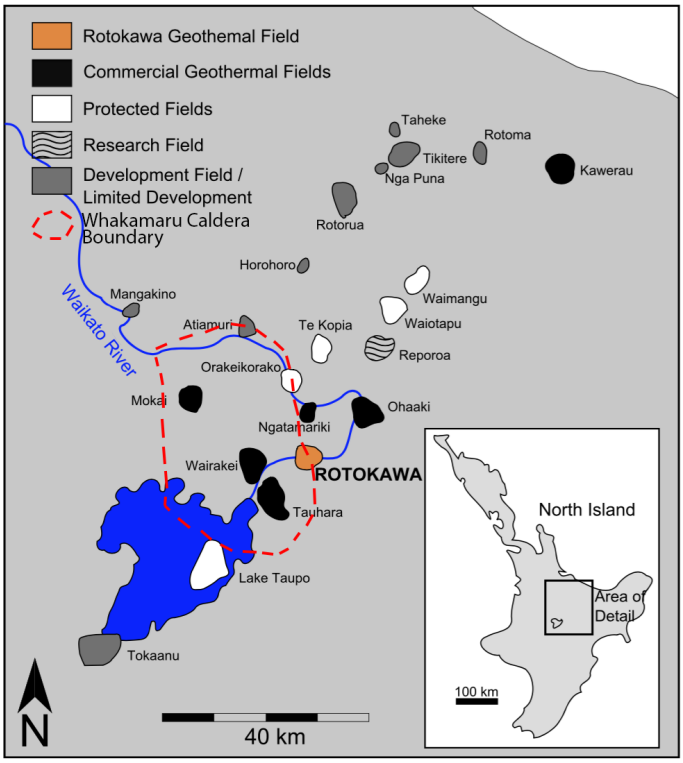

Figure 1.2: Location of Rotokawa Geothermal Field relative to other geothermal fields in the Taupo Volcanic Zone, figure originally in Siratovich et al. (2014) with added Whakamaru Caldera boundary from Brown et al. (1998)

1.2 Rotokawa Geothermal Field

The Rotokawa Geothermal Field (RGF) is situated in the central zone of TVZ and is approximately 10 km north-east of Taupo township (Figure 1.2). It is located within the Whakamaru Subdomain (Rowland and Sibson, 2001) and on the boundary of the Whakamaru Caldera (Figure 1.2). Based on timing of hydrothermal eruptions, the modern RGF geothermal system is estimated to be up to 20,000 years old (Krupp and

Seward, 1987; Vucetich and Howorth, 1976).

1.2.1 Surface features

Key surface features are shown in Figure 1.3. Most of RGF is sited south of the Waikato River. Rock types at the surface of the RGF include rhyolite, pumice alluvium, Wairakei breccia and hydrothermal eruption breccias (Rae, 2007; McNamara et al., 2015, and references there in).

The northern area is predominantly scattered rhyolite domes surrounded by pumice breccias. From the south, northeast trending structural lineaments are presented by hydrothermal eruption vents, including Lake Rotokawa (Rae, 2007) (Figure 1.3).

On the northern shores of Lake Rotokawa, surface alteration (acid sulphate style) occurs including native sulphur, kaolinite, smectite, silica residue, alunite, cinnabar and arsenic precipitates (Rae, 2007). Significant native sulphur accumulation (exceeding 2.6 Mt in the upper 20 m) is present beneath and adjacent to Lake Rotokawa (Rae, 2007).

There are numerous surface traces providing evidence of structural activity in the area, which have been identified and modelled. An example is the northeast-southwest striking active faults (Figure 1.4). The lineation and alignment of eruption vents further suggest structural alignment control (McNamara et al., 2015).

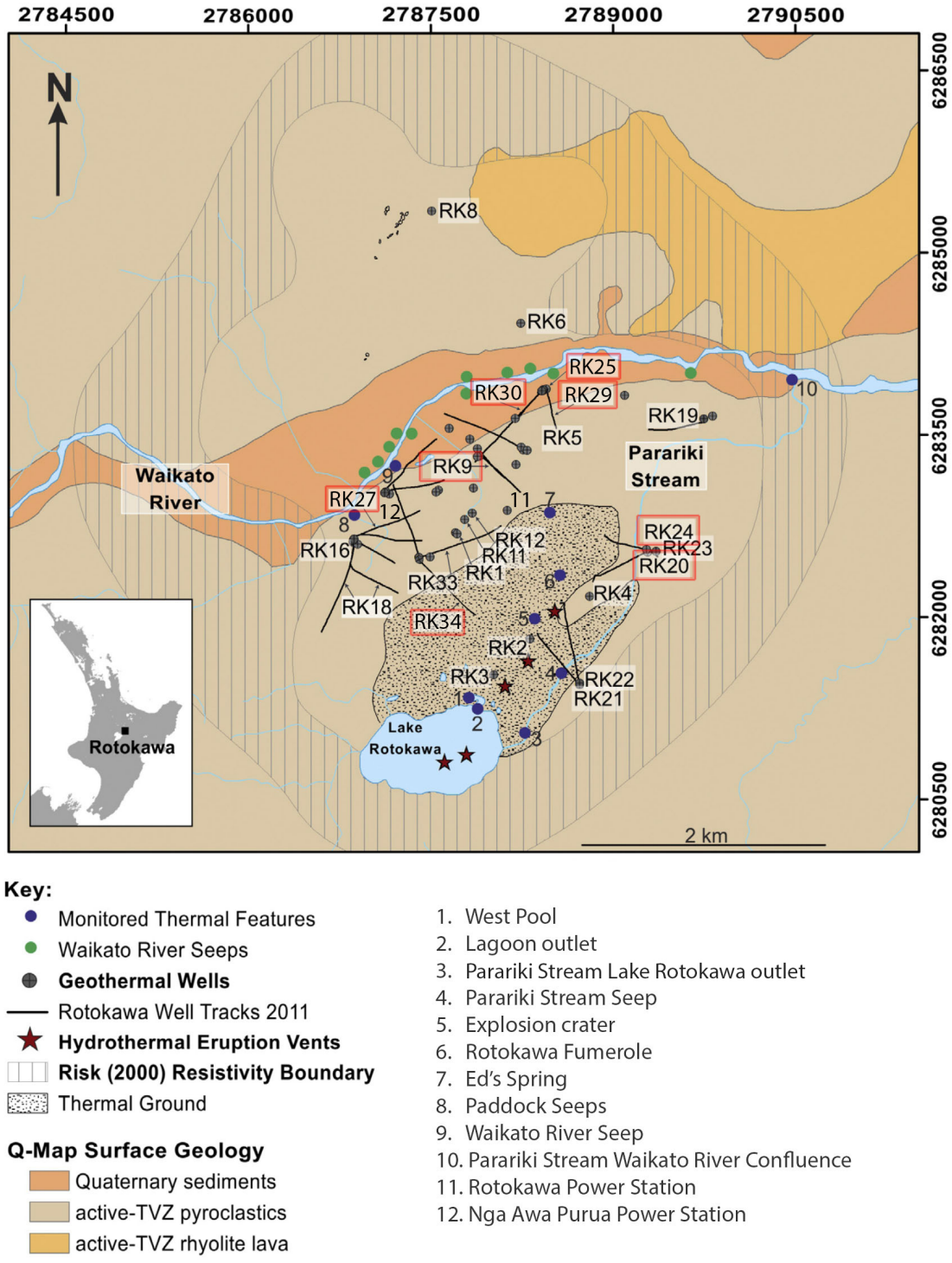

Figure 1.3: Map of Rotokawa geothermal field with key features, including resistivity boundary (Risk, 2000), production and injection wells, surface geological and hydrothermal features, and Rotokawa I and Nga Awa Purua power stations. Samples tested in this project are from the wells highlighted in red. Original figure from McNamara et al. (2015). Well labels for RK25, RK27, RK29, RK30 and RK34 were added from the MRP well reports.

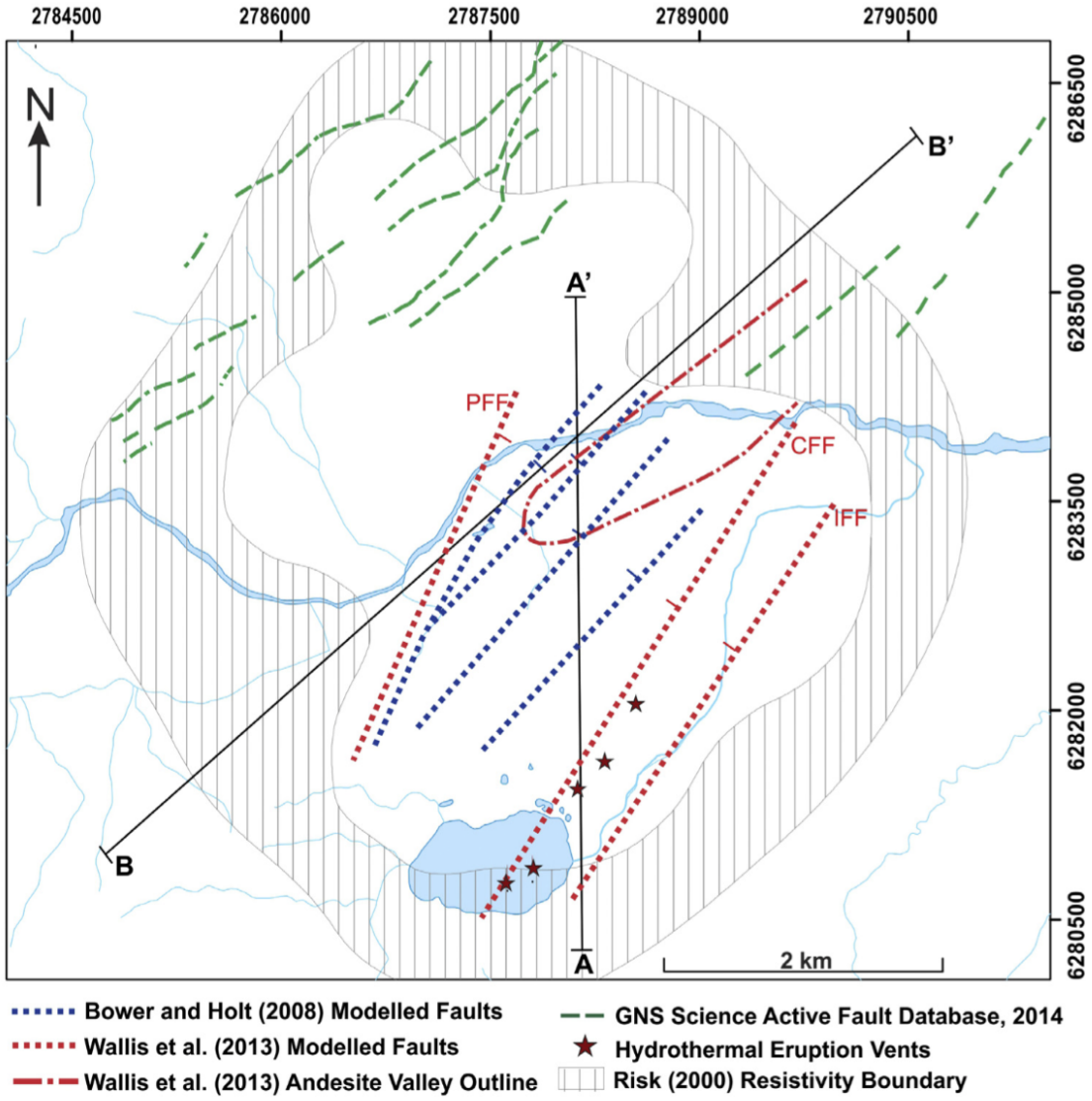

Figure 1.4: Map of the Rotokawa Geothermal Field showing active faults from GNS Active Fault Data Base (2014), modelled structures from Bowyer and Holt (2008), and modelled structures from Wallis et al. (2013) (1 = Production Field Fault, 2 = Central Field Fault, 3 = Injection Field Fault). A-A' is the location of the cross section in Figure 1.5 and B-B' is the location of a geophysics cross section in McNamara et al. (2015). Figure and caption from (McNamara et al., 2015).

1.2.2 Subsurface features

A generalised stratigraphy of the RGF is tabulated below (Table 1.1). Detailed lithological variation will be presented in Chapter 3.

Table 1.1: Rotokawa Geothermal Field general stratigraphy as described by Rae (2007).

Formation	**Thickness Range**	**Lithology**
Superficial (incl. Oruanui Formation)	10-30 m	Unaltered and thermally oxidised pumice tuff, rhyolite lava lithic clasts and unaltered quartz and feldspar crystals
Huka Falls Formation	15-150 m	Fine sandstone and siltstone with some pumice rich subunits.
Parariki Breccia	20-220 m	Strongly altered, quartz-feldspar rich tuffaceous breccia with a silty-clay matrix
Waiora Formation	90-550 m	Crystal-rich, hornblende-bearing vitric tuff
Rhyolite Lava and Breccia	110-660 m	Crystal-poor, rhyolite lava and breccia
Wairakei Ignimbrite	200-390 m	White, crystal-rich, non to densely welded ignimbrite. Large quartz crystals are often heavily embayed
Waikora Formation	10-250 m	Rounded to sub-rounded greywacke and argillite gravels.
Tahorakuri Formation	20-250 m	White, crystal-vitric-lithic tuff
Rotokawa Andesite	865-2190 m	Mottled, pale green and reddish purple, pyroxene-bearing andesite lava.
Greywacke Basement	-	Dark to pale grey, weakly metamorphosed argillite and fine silty sandstone

The subsurface geology is complex and is the result of regionally extensive northeast trending faulting followed by post basement volcano-stratigraphic sequences (Rae, 2007). The detailed cross section in Figure 1.5 illustrates the central field fault, along with the stratigraphic complexity and geochemical processes.

A full description of the RGF subsurface geology has been given in McNamara (2015) and references therein.

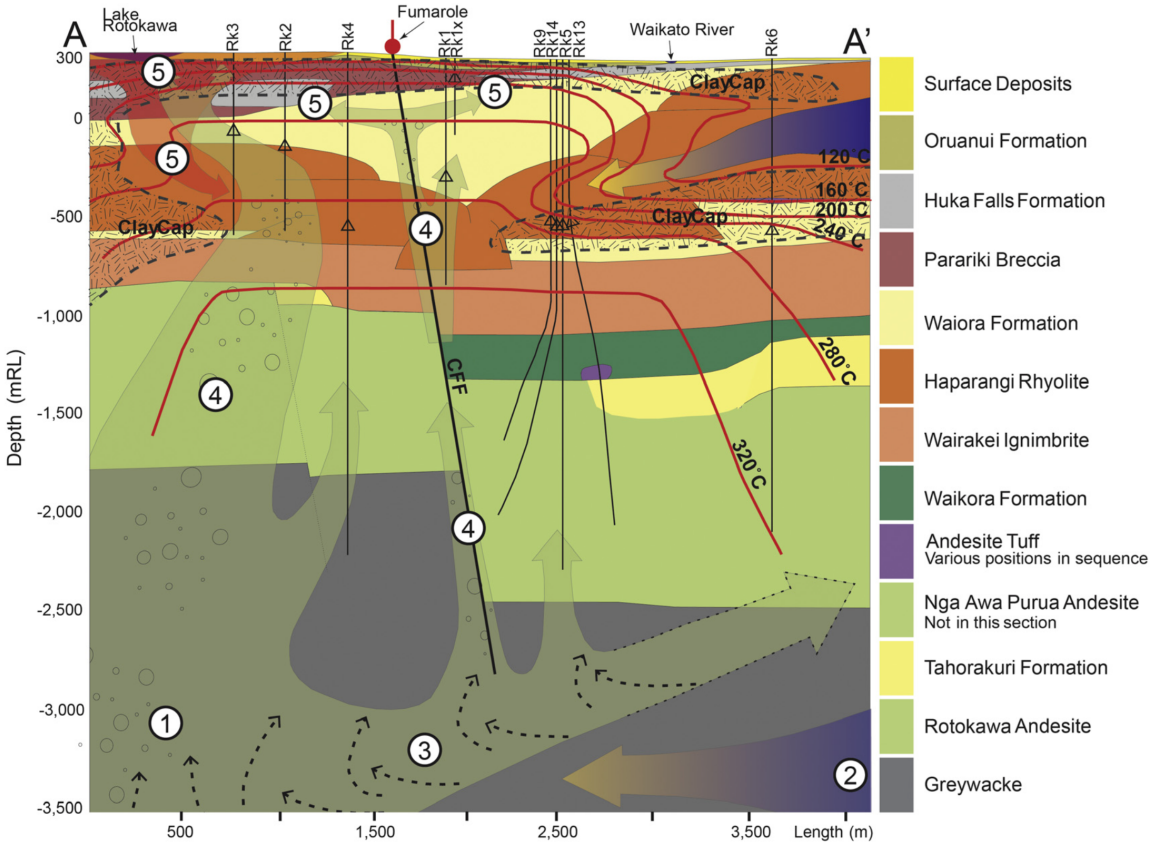

Figure 1.5: Cross section of the Rotokawa Geothermal Field (A–A' as shown in Figure 1.4) showing geological units, well locations, clay cap, isotherms, the Central Field Fault, and geochemical processes in the reservoir (1=hot two-phase upflow, 2 = deep conductively heated groundwater (up to 290°C), 3 = dilution and mixing with the deep conductively heated groundwater, 4 = adiabatic boiling, 5 = steam heated groundwater). Adapted from Winick et al. (2011). Original Figure and caption from McNamara et al. (2015).

The RGF has three, geochemically distinct aquifers; shallow, intermediate and deep. The shallow aquifer is single phase liquid (with some localised areas of boiling), the intermediate aquifer has hot, two phase geothermal fluids and the deep aquifer is a high temperature, convecting geothermal reservoir (Sewell et al., 2012; Winick et al., 2011)

For the most part, each aquifer is separated by impermeable layers with local zones of interconnection (McNamara et al., 2015). Faulting and large scale fracturing is suggested to be the main conduit for fluid flow through these aquifers (Rae, 2007).

1.2.3 Rotokawa development history

The Ministry of Works on behalf of the New Zealand government carried out exploratory drilling from 1965 to 1986, confirming the large, high temperature geothermal resource. In 1993, resource consent was granted and over the following four years Rotokawa I Power Plant was constructed (an Ormat geothermal combined cycle station). The power station was commissioned in 1997 with an installed capacity of 29 MWe, followed by an expansion to 34 MWe in 2003.

A second power station, Nga Awa Purua, began in 2008 with the drilling of wells RK19 to RK33. The triple flash plant was commissioned in 2010 (McLoughlin et al., 2010) adding another 140 MWe, and bringing the total field capacity to 174 MWe (McNamara et al., 2015). This is approximately 3% of New Zealand's annual power generation (Horie and Muto, 2010; Siratovich et al., 2014).

Because of the amount of development at Rotokawa and its significance to New Zealand's power generation, it has had considerable attention from researchers (McNamara et al., 2015). Geological, conceptual and numerical modelling of the field have been the key focus areas for research (e.g. Quinao and Azwar, 2012; Sewell et al., 2012).

1.3 Research aims and objectives

The objective of this thesis is to carry out a systematic physical and mechanical property study of rocks from Rotokawa Geothermal Field, under laboratory conditions. From the results of the laboratory testing, the following research aims and objectives will be answered:

- Investigate the relationship between matrix permeability and connected porosity and determine the role microstructure has on this relationship.
- Determine the effect microstructure has on the behaviour of sample rocks during triaxial strength testing.
- Determine if ultrasonic wave velocities relate to other parameters, such as porosity and permeability. Can ultrasonic wave velocities be used in the field for estimation of these parameters?
- Determine what the effect increasing confining stress has on matrix permeability. Investigate what role the microstructure of each sample has on how sensitive it is to increased confining stress.

- Develop a lithostatic model and use this to determine the in situ permeability for each sample. Investigate whether there is a relationship between depth and in situ permeability.
- Relate how this research is beneficial to geothermal power generation.

1.4 Thesis organisation

This thesis is divided into five chapters. Following the Introduction, Chapter 2 outlines the methods used to prepare samples, laboratory testing, lithostatic model calculation and data processing. In Chapter 3 the results of the collected data are presented, including empirical relationships and anomalies. Chapter 4 provides in depth analysis and discussion of the results, along with how these relate to geothermal power generation. Chapter 5 summarises the conclusions presented throughout the thesis, in particular those from Chapter 4.

Chapter 2

Methodology

Sample preparation and testing was carried out on pieces of core supplied by Mighty River Power (MRP) from their Rotokawa core shed. The core pieces were from eight wells across the field (RK09, RK20, RK24ST1, RK25, RK27, RK29, RK30 and RK34) and from various depths (501 m to 2606 m below ground level). This ensured the data collected was from varying lithological units across the field.

Table 2.1 provides a numbered system for each prepared sample set (four samples make up each set), along with well number, depth and lithological unit. Testing and preparation was carried out at the University of Canterbury (UC) Department of Geological Sciences unless otherwise stated.

Table 2.1: General information about each sample provided by Mighty River Power

Depth (m)	Well #	Rock type	Sample set
501	RK34	Rhyolite breccia	16
905	RK09	Rhyolite lava	1
1113	RK30	Pumice ignimbrite	15
1511	RK09	Fine-grained sandstone conglomerate	3
1821	RK24ST1	Hydrothermally-altered brecciated andesite	7
1852	RK27	Andesite breccia	11
1854	RK27	Andesite lava clast	12
2081	RK29	Andesite lava	14
2120	RK27	Andesite lava	4.2
2147	RK27	Andesite lava	13
2200	RK25	Andesite breccia	10
2320	RK30	Andesite breccia	21.4
2606	RK20	Hydrothermally-altered fine grained sandstone	6

2.1 Sample preparation

Plugs of rock were drilled from the core pieces using a high precision diamond tipped Wendt Forvet glass drill, supplied by Dr Mike Heap from Université de Strasbourg, France.

The samples were drilled to 20 mm in diameter allowing for efficient use of the permeameter (a sample with this diameter was able to be inserted from the bottom of the apparatus, without draining hydraulic fluid each time). Each sample was cut as close to 40 mm in length as possible (i.e. twice their diameter). A set of four individual samples were drilled from each well and depth; a total of 44 samples. A further nine samples, prepared by Dr Paul Siratovich, were also used. Due to time constraints and equipment availability, only two samples from each set could be tested in the permeameter during the course of the program.

A diamond encrusted rotary grinder was used to square off both ends to ensure the permeameter gas distribution platens sat flush and to remove any chips from the edges of each sample.

The samples were fully submerged in deionised water and placed in a Sandelin Sonorex ultrasonic bath in order to remove any dust particles and debris left over from drilling and grinding.

2.2 Porosity and density measurements

The two International Society for Rock Mechanics (ISRM) standard techniques were used to determine the porosity and density of each sample; the caliper technique and the buoyancy technique (Hudson and Ulusay, 2007). Because three sample sets had issues with swelling clays, they were tested using a gas pycnometer.

2.2.1 Saturation and buoyancy technique

Three measurements of mass were taken for each sample on scales accurate to 0.001 grams:

- Saturated mass
  - Each sample was saturated using deionised water in a dessicator under 100 kPa vacuum for 24 hours.
- Submerged mass
  - Each saturated sample was hung on a hook that was attached to the bottom of the scales and fully submerged in deionised water.
- Dry/sample mass
  - Each sample was oven dried for 48 hours at 105°C.

Well reports prepared by GNS Science for Mighty River Power (MRP) were consulted prior to testing (Wood and Rosenberg, 1997; Milicich et al., 2008; Ramirez and Rae, 2009; Rae et al., 2009, 2010; Sanders et al., 2015). Provided in these reports were methylene blue absorption plots, which help identify swelling clays within core samples. Sample sets 1, 11, 15, and 16 had swelling clays present.

Swelling clays react when they come into contact with water, producing inaccurate results. Instead of deionised water, dichloromethane (a non-polar fluid which does not react with swelling clays) was used for these three sample sets. This same fluid was used for similar samples in Wyering et al. (2014). Dichloromethane is very toxic and boils at 39.6°C, so testing was carried out in one of the SABRE Laboratory's fume cupboards, under the supervision of Chris Grimshaw.

Equations 2.1, 2.2, 2.3 and 2.4 were used to calculate the desired rock properties (Hudson and Ulusay, 2007):

$$V = \frac{M_{Sat} - M_{Sub}}{\rho_w} \tag{2.1}$$

$$V_v = \frac{M_{Sat} - M_S}{\rho_w} \tag{2.2}$$

$$n = \frac{100V_v}{V}\% \tag{2.3}$$

$$\rho_d = \frac{M_S}{V} \tag{2.4}$$

where:

V = Bulk volume (cm^3)
M_{Sat} = Saturated mass (g)
M_{Sub} = Submerged mass (g)
ρ_w = Density of fluid - water or dichloromethane (g/cm^3)
V_v = Pore volume (cm^3)
M_S = Sample mass - dry mass (g)
n = Porosity (%)
ρ_d = Rock density (g/cm^3)

2.2.2 Saturation and caliper technique

The length and diameter of each sample was measured using a set of calipers accurate to 0.01 mm. In order to take into account potential small variations within each sample, three measurements were taken at different locations and averaged. Equation (2.5) was used to calculate the bulk volume, V. All other equations are the same as the buoyancy technique.

$$V = \pi r^2 \times L \tag{2.5}$$

where:

V = Bulk volume (cm^3)
r = Radius of the sample (cm)
L = Length of the sample (cm)

2.2.3 Pycnometer Measurement

The results for sample sets 1, 11 and 16 were inconsistent with the rest of the data suggesting the dichloromethane measurements were inaccurate. A gas pycnometer was used to attempt to remove these inconsistencies. The pycnometer is an apparatus for measuring porosity and density that uses nitrogen gas as the saturation fluid and does not react with swelling clays.

Analysis was performed on an Ultrapycnometer 1000 by Quantachrome Instruments at the University of Waikato, New Zealand. Operating temperature was 25.7-26.2° C and the target pressure was 18 PSI.

2.3 Lithostatic stress model

A lithological stress model was developed in order to predict the in situ effective stress applied to each sample in the field. The method for developing the model was similar to that used in Cant (2015). Thickness and sequence of the rock units for each of the eight wells was collated from the well logs produced by GNS Science (Wood and Rosenberg, 1997; Milicich et al., 2008; Ramirez and Rae, 2009; Rae et al., 2009, 2010; Sanders et al., 2015).

2.3.1 Rock density

Estimates of rock densities were either averaged from those calculated in this thesis or extrapolated from literature. Table 2.2 contains the density values used for each rock type that is present in each well.

Table 2.2: Lithostatic rock density information. 1) Density estimate is from the TVZ but not from Rotokawa. 2) Density estimate is from a similar rock description outside TVZ. 3) Density estimated from a standard rock description

Stratigraphic unit	Rock type	Source	Density (kg/m^3)
Oruanui	Pumice tuff and rhyolite lava	(Palmer, 1982)[2],	1450
Huka Falls	Siltstone and sandstone	(Read et al., 2001)[1]	1033
Parariki Breccia	Tuffaceous breccia	(Wohletz and Heiken, 1992)[3]	2100
Tuff siltstone	Tuff Siltstone	(Wohletz and Heiken, 1992) [3]	2000
Waiora	Tuff	(Vutukuri and Lama, 1940)[3]	2140
Whakamaru Ignimbrite	Ignimbrite	(Vutukuri and Lama, 1940)[3],	2045
Rhyolite Lava	Rhyolite lava	This thesis	2397
Rhyolite Breccia	Rhyolite breccia	This thesis	2005
Rhyolite lava and breccia	Rhyolite	This thesis	2201
Wairakei Ignimbrite	Ignimbrite	This thesis	1913
Waikora formation	Greywacke conglomerate	This thesis	2509
Tahorakuri Formation	Lithic tuff	(Cant, 2015)[1], (Wyering et al., 2014)[1]	2360
Andesite Breccia	Andesite Breccia	This thesis	2424
Andesite Lava	Andesite lava	This thesis	2561
Rotokawa Andesite	Andesite	This thesis	2493
Greywacke basement	Greywacke	This thesis	2682

2.3.2 Fluid density

Temperature affects water density, therefore it should be accounted for in the lithostatic model. For each rock unit, an average water temperature was calculated using temperature logs supplied by MRP. Equation (2.6) was used to calculate the water density for each unit (McCutcheon et al., 1993). Figure 2.1 demonstrates how significant the difference in density of water is with an increase in temperature and excluding it decreases the effective stress.

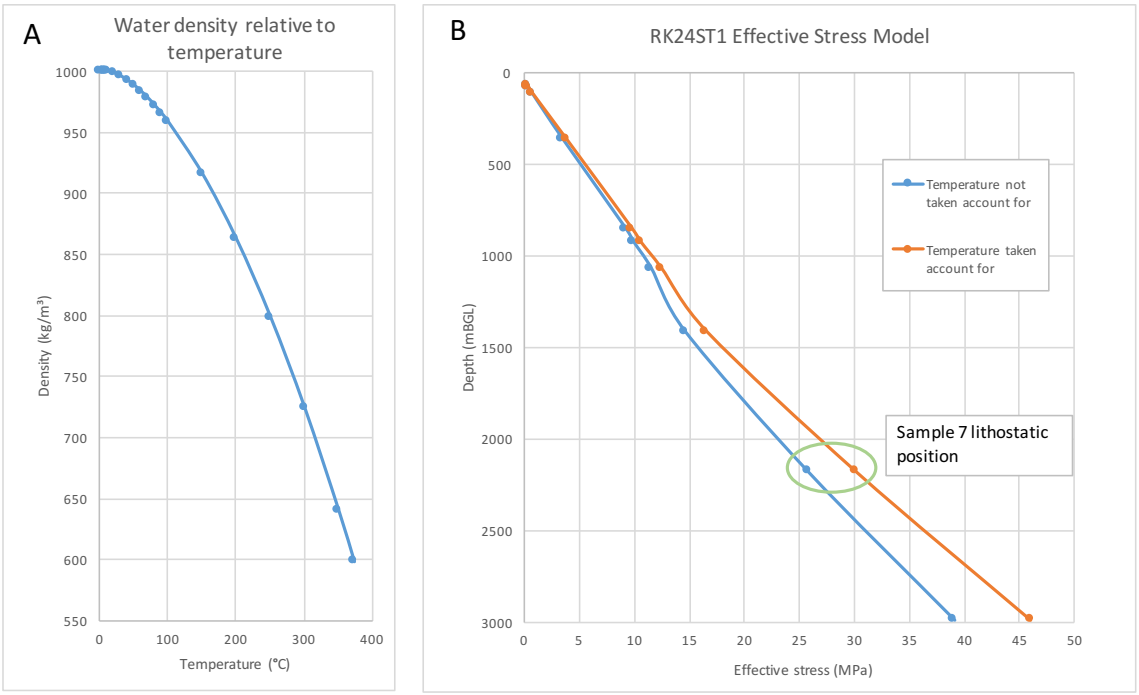

Figure 2.1: A) Water density decreases as the temperature increases in a quadratic fashion. B) The effect temperature has on the lithostatic model of RK24ST1

$$\rho_w = 1000\left[1 - \frac{T + 288.9414}{508929.2(T + 68.12963)}(T - 3.9863)^2\right] \tag{2.6}$$

where:

ρ_w = Density of water (kg/m^3)
T = Temperature (°C)

Initially a method was trialled which took into account the lithostatic pressure on water. Equation (2.6) assumes water remains in aqueous phase because of sufficient

pressure. When in aqueous phase, pressure has little effect on the density of water (i.e. it is incompressible) and is typically ignored (McCutcheon et al., 1993). This prompted the decision to use the simpler approach using equation (2.6).

2.3.3 Lithostatic effective stress equations

Using Equations (2.7), (2.8) and (2.9) below, the estimated effective lithostatic stress was calculated for each unit and well. A cumulative effective stress was used to estimate in situ effective stress of each sample.

$$\sigma' = \sigma - u \tag{2.7}$$

$$\sigma = \rho_l g h \tag{2.8}$$

$$u = \rho_w g h \tag{2.9}$$

where:

σ' = Effective stress (MPa)
σ = Lithostatic stress (kg/m^3)
ρ_l = Density of lithological unit (kg/m^3)
u = Pore pressure (MPa)
ρ_w = Density of water (kg/m^3)
g = Gravitational force (m/s^2)

2.3.4 Assumptions

Several assumptions are made with this lithostatic model, including:

- Each unit is considered homogeneous, but can show slight variation. Averaged densities for each unit were used to account for as much variation as possible.
- The hydrostatic component assumes a continuous linked aquifer and the entire system is "wet" with no gas present and each unit is at the same temperature throughout.
- The density calculation assumes pure water rather than brine.

2.4 Thin section analysis

Thin section analysis was carried out on 12 polished thin sections prepared by Rob Spiers. Representative rock fragments were used as the tested samples could be required for future research.

2.4.1 Polarised light microscopy

Polarised light microscopy was carried out on a Leica DM2500 P microscope and images were captured on the attached DFC295 camera. Thin sections were examined to highlight key minerals, textures and alterations throughout.

Key minerals identified from each thin section can be found in the digital appendix. Each thin section was categorised by level of alteration; none, minor, moderate or high. These categories were selected in accordance with the similar detailed thin section descriptions in the GNS reports.

2.4.2 Scanning electron microscope imaging

Each thin section was carbon coated for analysis using a JEOL JSM-7000F Field Emission Scanning Electron Microscope (SEM) in the Mechanical Engineering Department (UC).

The electron back scatter detector within the SEM produces images that contrast elements of different atomic weights; high atomic weight produces bright pixels whereas low atomic weight produces dark pixels. This illustrates the difference between minerals (high atomic weight) and pores/cracks filled with resin (low atomic weight).

Rather than calculating quantitative values for thin section porosity and fracture density (as in Cant (2015) and Siratovich et al. (2014)), qualitative descriptions of the SEM images are used to help indicate data relationships.

2.5 Permeability testing

Permeability testing was carried out on a PDP-200 Pulse Decay Permeameter in the Engineering Geology Laboratory (UC) (Figure 2.2).

The PDP-200 has the capability to biaxially confine samples up to 60 MPa, as a proxy for increased lithostatic stress. It can also increase the temperature of samples, but due to time constraints this was beyond the scope of this project. The apparatus has a coil heater and two fans to keep the temperature inside the system constant at 30°C.

Prepared samples were inserted into the apparatus and the desired confining stress was applied. The sample sits in an impermeable rubber sleeve, which applies the confining stress without hydraulic fluid reaching the sample. Most samples were tested from 5-30 MPa, increasing by 5 MPa during each test. When the calculated lithostatic effective stress was low, samples were only tested to 15 MPa.

For each test, compressed nitrogen gas was used as a proxy for pore pressure. The gas was left to soak for sufficient time for all the pore space in the sample to become saturated with gas. The downstream gas reservoir was then bled to create a pressure difference above and below the sample. The change in differential pressure is monitored over time. Equation 2.10 (Brace et al., 1968), is a modified version of Darcy's Law and the PDP200 software used this to calculate the gas permeability.

$$k_{gas} = \left(\frac{2\eta L}{A}\right)\left(\frac{V_{up}}{{P_{up}}^2 - {P_{down}}^2}\right)\left(\frac{\Delta P_{up}}{\Delta t}\right) \tag{2.10}$$

where:

k_{gas} = Gas permeability (mD)
η = Viscosity of the nitrogen gas (Pa s)
L = Length of the sample (cm)
A = Cross sectional area of the sample (cm^2)
V_{up} = Volume of gas in the upstream reservoir and piping (cm^3)
P_{up} = Pressure of gas in the upstream reservoir and piping (PSI)
P_{down} = Pressure of gas in the downstream reservoir and piping (PSI)
t = Elapsed time

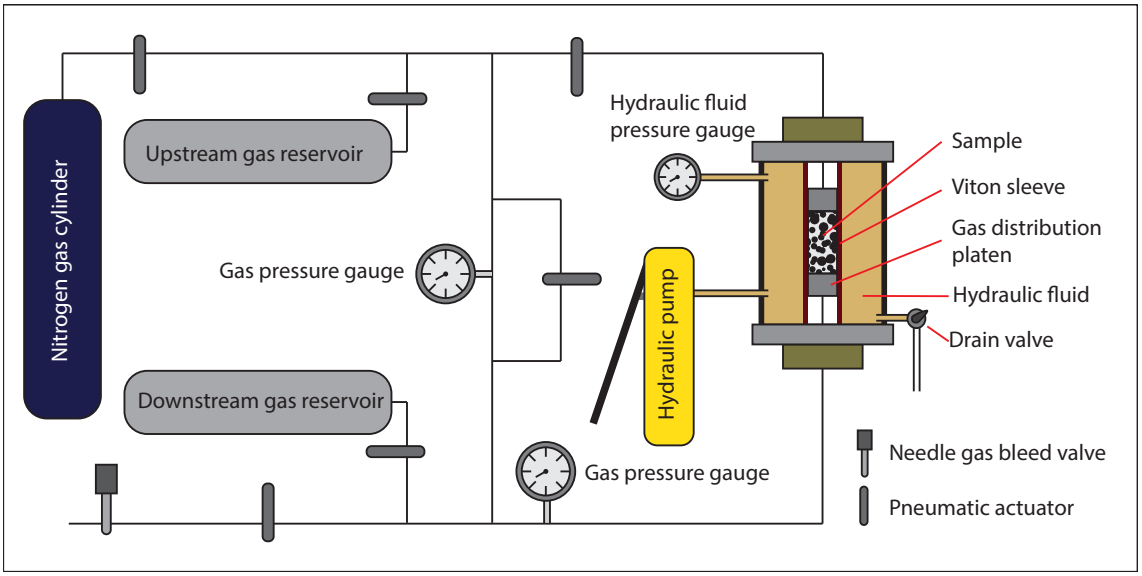

Figure 2.2: A schematic diagram of the PDP-200 permeameter.

2.5.1 Klinkenberg correction

When each test is running, gas tends to flow faster at the grain boundaries than water would, a phenomenon known as gas slippage. In order to account for this, the Klinkenberg correction is applied; equation 2.11 (Klinkenberg, 1941). This requires a series of four tests with varying pore pressure, for each confining stress.

$$k_{true} = k_{gas}\left(1 + \frac{b}{P_{mean}}\right) \tag{2.11}$$

where:

k_{true} = True permeability (m^2)
k_{gas} = Gas permeability (m^2)
b = Klinkenberg slip factor
P_{mean} = Mean pore pressure (PSI)

Inverse mean pore pressure was plotted against permeability and the y-intercept of the best fit line is the true permeability (Figure 2.3). A minimum correlation co-efficient of 0.9 was determined to ensure test results were consistent.

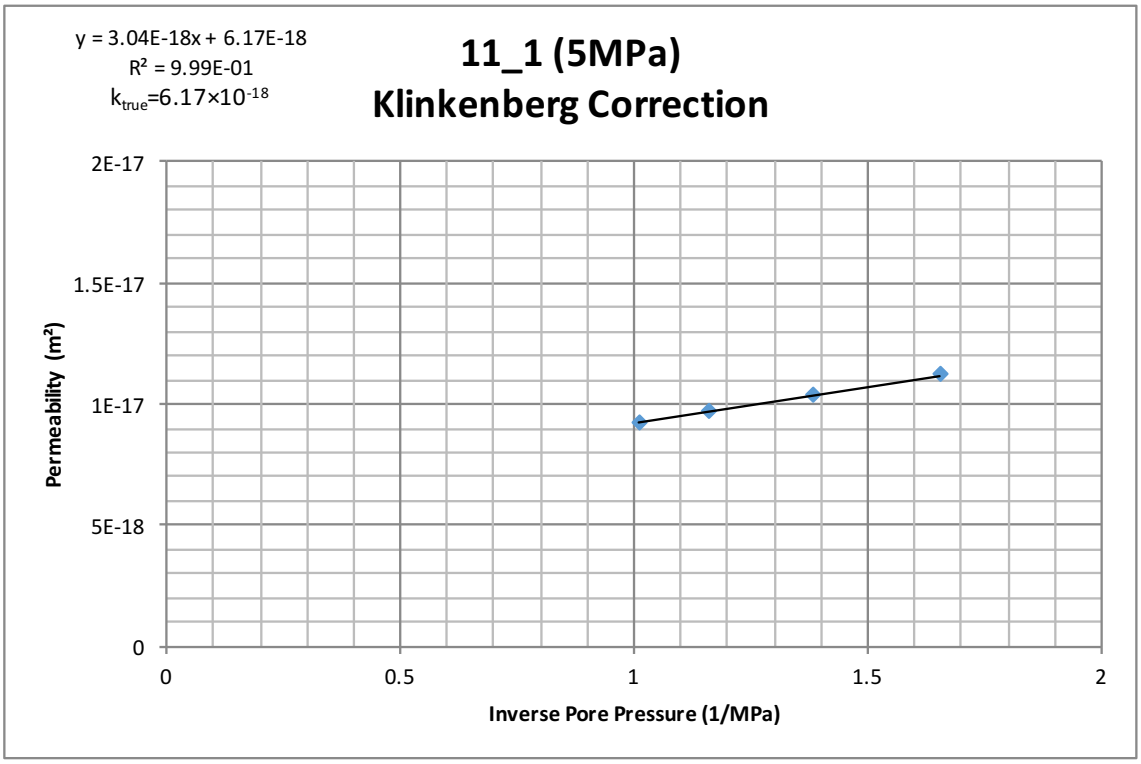

Figure 2.3: Example of a Klinkenberg Correction plot; Sample 11_1 at 5MPa confining stress

2.6 Ultrasonic wave velocity testing

Ultrasonic wave velocity measurements were carried out on each sample using a Computer Aided Ultrasonic Velocity Testing System (CATS ULT-100) manufactured by Geotechnical Consulting and Testing Systems (GCTS). Sample sets 11 and 14 were tested in Université de Strasbourg, France by Dr Marlène Villeneuve.

Honey was used as a coupling medium to ensure a good contact between each sample and the piezoelectric tranducer platens, which transmit and measure the arrival time of shear and compressional waves. A load of 30 kg was applied above the top platen ($\sim$1 MPa vertical confining stress) to further ensure adequate contact. Figure 2.4 shows the equipment setup. Ultrasonic wave velocity measurements were carried out after permeability was tested to prevent introducing honey into the permeameter system.

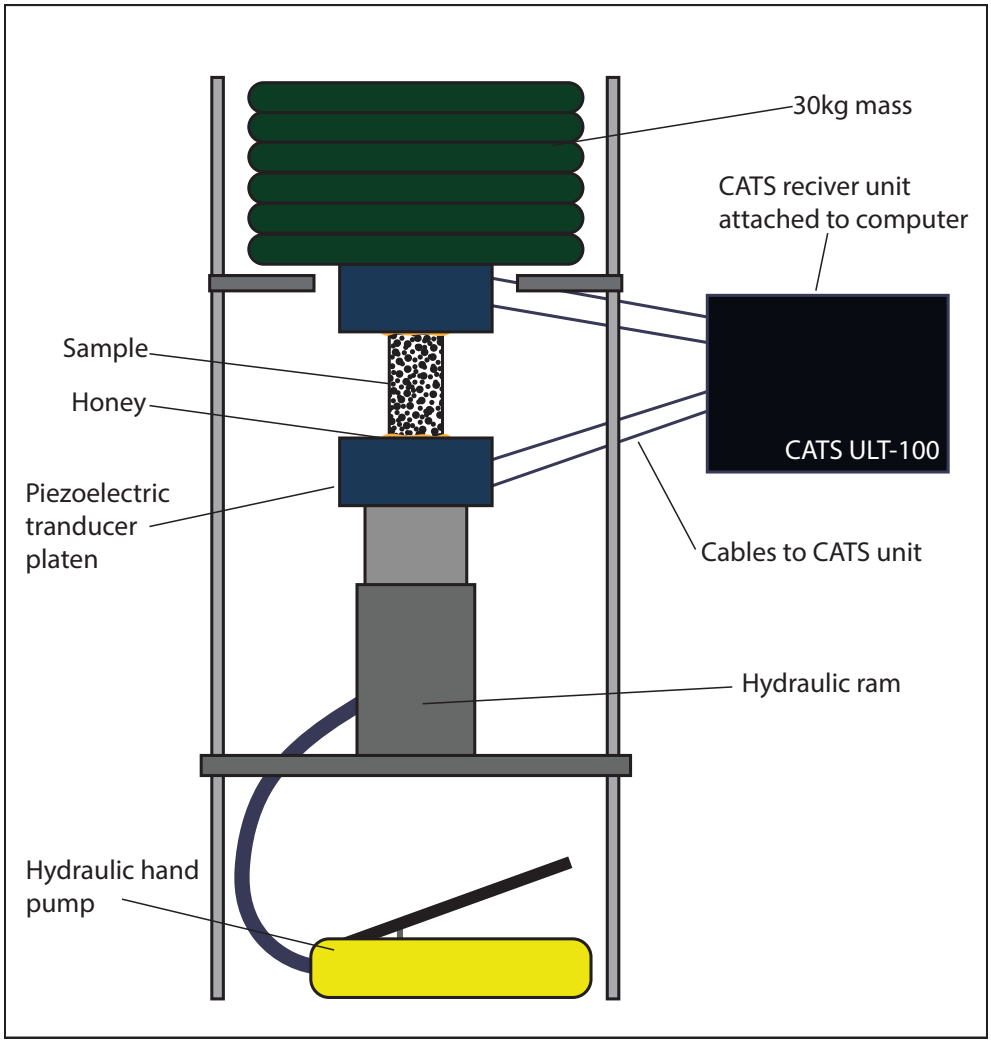

Figure 2.4: Ultrasonic wave velocity testing equipment set up

Equations (2.12) and (2.13) were used to calculated the Poisson's Ratio and Young's Modulus (Guéguen and Palciauskas, 1994).

$$v = \frac{{V_p}^2 - 2{V_s}^2}{2({V_p}^2 - {V_s}^2)} \tag{2.12}$$

$$E = \frac{\rho {V_s}^2(3{V_p}^2 - 4{V_s}^2)}{{V_p}^2 - {V_s}^2} \tag{2.13}$$

where:

v = Poisson's Ratio

V_p = P-wave velocity - compressional (m/s)
V_s = S-wave velocity - shear (m/s)
E = Young's modulus (Pa)
ρ = Density(kg/m^3)

2.7 Triaxial testing

Triaxial testing was carried out on two samples from each of sample sets 11 and 14 by Dr Marlène Villeneuve at the Université de Strasbourg, France. The testing followed the conventional method (i.e. $\sigma 1 > \sigma 2 = \sigma 3$) described in Heap et al. (2014a). The testing was carried out at constant strain rate ($1.0 \times 10^{-5} s^{-1}$).

Experiments were performed in the conventional triaxial deformation apparatus (Figure 2.5) at an effective pressure of 40 MPa and 70 MPa. Axial stress and strain were monitored continuously using a load cell. Porosity reduction (used as a proxy for volumetric strain) was monitored using a pore pressure intensifier.

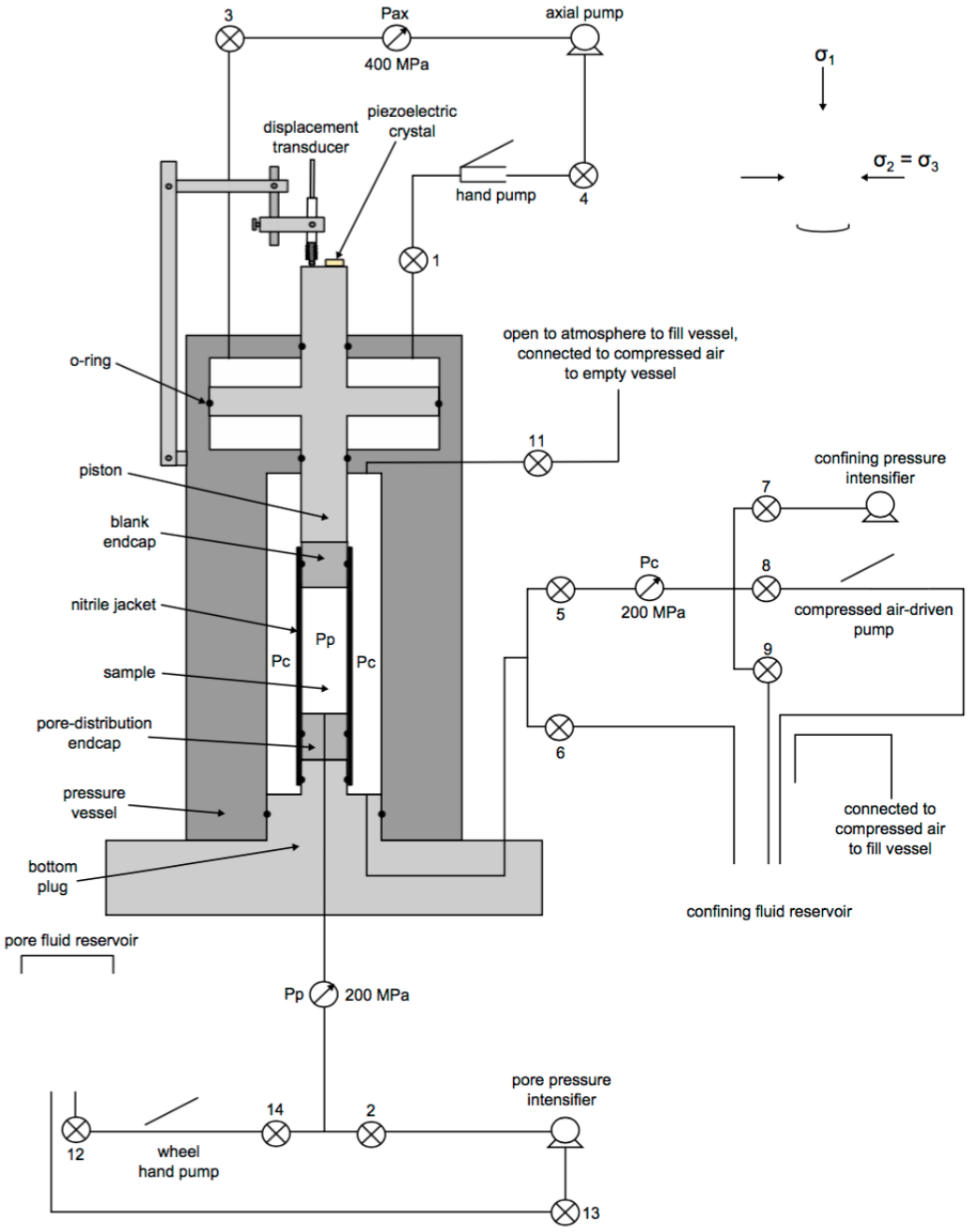

Figure 2.5: Schematic diagram of the triaxial deformation apparatus at the Laboratoire de Déformation des Roches, Université de Strasbourg. Schematic is not to scale. Caption and figure originally from Heap et al. (2014a)

Chapter 3

Results

3.1 Samples

Table 2.1 provides general information for each prepared sample set, including which well and depth it was from, the rock type and the associated sample number. The information in this table was sourced from the GNS well reports (Wood and Rosenberg, 1997; Milicich et al., 2008; Ramirez and Rae, 2009; Rae et al., 2009, 2010; Sanders et al., 2015).

3.2 Porosity and density

Table 3.1 contains the average porosity and density data for the two methods; caliper and buoyancy. There is minimal difference between each method (less than 2%) which is likely be due to human error.

Table 3.1: Average porosity and dry density data for each sample set from the two testing methods: caliper and buoyancy.

	Average Porosity (%)			Average Dry Density (kg/m^3)		
Sample Set	Buoyancy	Caliper	Difference (%)	Buoyancy	Caliper	Difference (%)
1	8.9	9.0	1.4	2341	2383	1.4
3	9.8	9.7	1.1	2509	2474	1.1
6	3.9	3.8	1.5	2682	2642	1.5
7	8.6	8.4	1.0	2579	2545	1
10	12.9	12.7	1.4	2429	2388	1.4
11	15.6	15.3	1.6	2334	2301	1.6
12	15.9	15.6	1.6	2355	2321	1.6
13	2.1	2.0	1.2	2804	2782	1.2
14	16.7	17.4	1.3	2266	2230	1.3
15	25.1	25.2	0.6	1912	1921	0.6
16	5.6	5.7	0.7	1972	2013	0.7
4.2	6.5	6.5	0.3	2594	2585	0.3
21.4	6.9	6.9	0.3	2579	2570	0.3

Figure 3.1 was used to validate the data; dry density and porosity would be expected to have a linear relationship. As can be seen in Plot A of Figure 3.1, there are three sets of outliers (circled). These are the samples tested using dicholormethane instead of water. The increase in the correlation coefficient from 0.46 to 0.97 suggests caution when relating this data to other parameters. Water was trialled for these samples too, but inconsistencies remained. Sample sets 1, 11 and 16 were tested using the pycnometer, but only sets 1 and 11 became consistent. The corrected values are presented in Plot B, where the outliers have also been removed. Sample sets 15 and 16 are left out of any subsequent plots showing porosity or density.

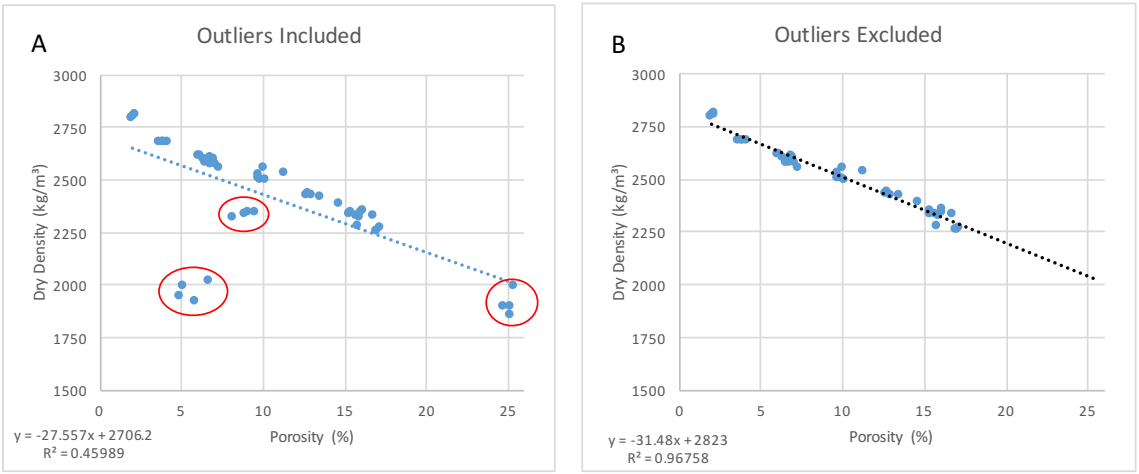

Figure 3.1: Porosity plotted against density.

Figure 3.2 shows the relationship between the depth of each sample and the corresponding porosity and density. There is weak correlation between increasing depth and decreasing porosity, and a moderate positive linear correlation between dry density and depth.

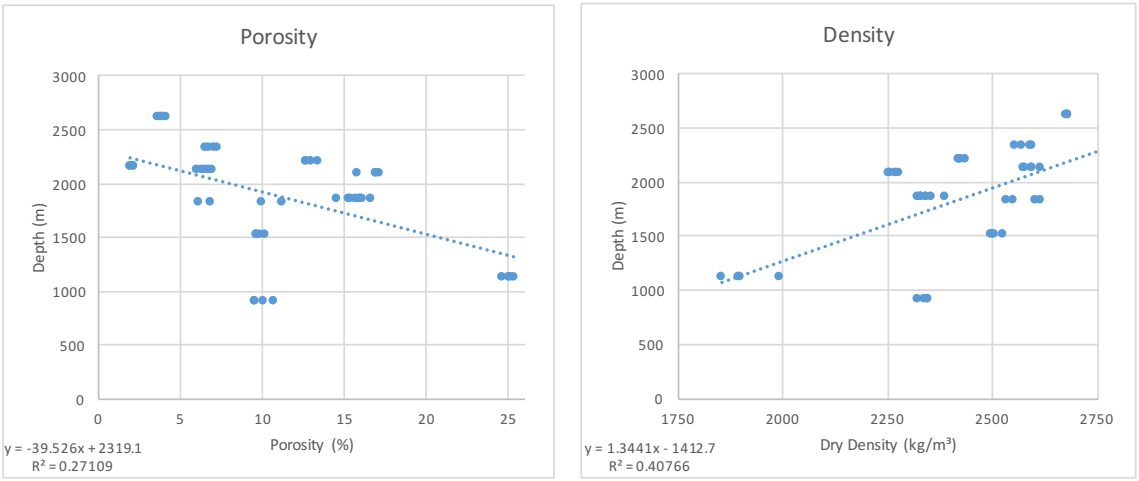

Figure 3.2: Porosity and density plotted against depth

3.3 Lithostatic stress model

Table 3.2 presents lithostatic models for each well. Separate tables were used because not all units were present in all wells.

Table 3.2: Lithostatic stress model for each well. D is the lower depth of each unit (metres below ground level). σ' is the cumulative stress calculated for the bottom of each unit.

RK34

D (mBGL)	Unit	σ' (MPa)
130	Oranui Formation	0.6
200	Parariki Breccia	1.4
495	Waiora Formation	5.0
610	Haparangi Rhyolite	6.5
1055	Waiora Formation	12.5
1165	Whakamaru Ignimbrite	13.9
1415	NAP Andesite	18.4
1455	Waikora Formation	19.1
1705	Tahorakuri Formation	23.2
1785	RKA	23.8

RK09

D (mBGL)	Unit	σ' (MPa)
30	Oranui	0.1
92	Huka Falls	0.2
422	Waiora	4.5
507	Rhyolite Breccia	5.5
937	Rhyolite Lava	12.1
1027	Waiora	13.3
1412	Wairakei Ignimbrite	17.9
1677	Waikora	22.6
2042	RKA	29.1

RK29

D (mBGL)	Unit	σ' (MPa)
72	Oranui	0.3
127	Huka Falls	0.4
327	Waiora	2.7
702	Haparangi Rhyolite	7.4
997	Waiora	11.1
1462	Wairakei Ignimbrite	16.7
1572	Tahorakuri	18.5
2076	RKA	27.5

RK20

D (mBGL)	Unit	σ' (MPa)
68	Oranui	0.3
83	Huka Falls	0.3
113	Parariki Breccia	0.7
133	Huka Falls	0.7
378	Waiora	3.7
868	Haparangi Rhyolite	9.7
943	Tuff siltstone	10.6
1013	Waiora	11.5
1388	Wairakei Ignimbrite	15.9
2333	RKA	32.7
2599	Greywacke	38.0

RK25

D (mBGL)	Unit	σ' (MPa)
70	Oranui	0.3
100	Huka Falls	0.3
310	Waiora	2.8
705	Haparangi Rhyolite	7.7
1010	Waiora	11.7
1410	Wairakei Ignimbrite	16.4
1685	Waikora	21.4
1810	Tahorakuri	23.4
2200	RKA	30.3
2697	RKA	39.1

RK24ST1

D (mBGL)	Unit	σ' (MPa)
68	Oranui	0.3
78	Huka Falls	0.3
118	Parariki Breccia	0.7
368	Waiora	3.8
853	Haparangi Rhyolite	9.8
928	Tuff Siltstone	10.6
1068	Waiora	12.5
1413	Wairakei Ignimbrite	16.6
2178	RKA	30.2
2985	Greywacke	46.0

RK30

D (mBGL)	Unit	σ' (MPa)
71	Oranui	0.3
111	Huka Falls	0.3
346	Wairoa	3.1
711	Haparangi	7.6
991	Waiora	11.3
1011	Andesite	11.6
1066	Waiora	12.4
1471	Wairakei Ignimbrite	17.2
1611	Waikora	19.7
1651	Tahorakuri	20.4
2051	RKA	27.4
2126	Tahorakuri	28.6
2132	RKA	28.7

RK27

D (mBGL)	Unit	σ' (MPa)
50	Oranui	0.2
55	Huka Falls	0.2
95	Parariki Breccia	0.7
130	Huka Falls	0.7
180	Waiora	1.3
225	Haparangi Rhyolite	1.8
850	Waiora	9.0
1395	RKA	18.5
1445	Tahorakuri	19.4
1635	Waikora	22.8
1787	Tahorakuri	25.2
2143	RKA	31.6

3.4 Thin sections

3.4.1 Polarised light microscopy

Thin section images can be found in the digital appendix. Table 3.3 provides the extent of alteration in each of the thin sections. The alteration is as described for comparable thin sections in the GNS reports (Wood and Rosenberg, 1997; Milicich et al., 2008; Ramirez and Rae, 2009; Rae et al., 2009, 2010; Sanders et al., 2015).

Table 3.3: Table of alteration strength in sample thin sections

Thin section	Well	Alteration
1	RK09	Weak
3	RK09	None-weak
6	RK20	Weak-moderate
7	RK24ST1	Moderate-high
10	RK25	High
11	RK27	High
12	RK27	High
13	RK2	Weak
14	RK29	Moderate-high
15	RK30	Weak-moderate
16	RK34	Moderate

3.4.2 SEM imaging

Five thin sections were analysed with the SEM; thin sections 1 (rhyolite lava), 6 (basement greywacke), 10 (andesite breccia), 11 (andesite breccia) and 14 (andesite lava). Porosity and permeability data for these sample sets is supplied in Table 3.4.

A key comparison in the data set is between 11 and 14. They both have similar porosity (within 2% of one another), yet permeability is nearly two orders of magnitude different. To ensure the measurements for sample set 14 were not due to equipment error, multiple permeameter tests were carried out, including at the Université de Strasbourg, France, where results remained consistent. Detailed discussion of the microstructure for these is provided in Chapter 4, along with corresponding SEM images.

Table 3.4: Porosity and permeability range and averages for sample sets 11 and 14

		Porosity (%)		Permeability (m^2)	
Set	Rock type	Range	Average	Range	Average
1	Rhyolite lava	9.6 - 10.7	10.0	2.26 - 2.66 $\times 10^{-18}$	2.46 $\times 10^{-18}$
6	Basement greywacke	3.6 - 4.1	3.8	3.78 - 3.90 $\times 10^{-19}$	3.84 $\times 10^{-19}$
10	Andesite breccia	12.4 - 13.2	12.7	3.91 - 6.86 $\times 10^{-18}$	5.39 $\times 10^{-18}$
11	Andesite breccia	14.8 - 15.3	15.1	6.17 - 8.40 $\times 10^{-18}$	6.93 $\times 10^{-18}$
14	Andesite lava	15.8 - 17.1	16.7	1.84 - 2.48 $\times 10^{-16}$	2.24 $\times 10^{-16}$

3.5 Permeability testing

Table 3.5 contains the permeability data for each tested sample at the varying confining stresses. Figure 3.3 is a plot of this data. It can be seen for most samples, an increased confining stress decreases the permeability. When preparing set 13, all samples contained macro-fractures so were not tested for matrix permeability. Sample set 15 (pumice ignimbrite) was tested, but the permeability was too high for the equipment's tolerance. Because sample set 6 had such low permeability, it was only tested to 20 MPa due to time constraints.

Table 3.5: Klinkenberg corrected permeability dataset

Confining Stress (MPa)	Permeability (m^2)							
	1_1	1_3	3_1	3_3	6_1	6_3	7_1	7_3
5	2.26274E-18	2.6625E-18	1.20942E-18	1.09748E-18	3.77729E-19	3.89811E-19	2.3328E-17	9.14678E-19
10	1.32911E-18	1.67903E-18	7.12349E-19	7.01037E-19	1.46068E-19	2.25188E-19	2.01025E-17	3.59739E-19
15	9.89043E-19	1.16854E-18	5.09865E-19	4.82325E-19	9.75814E-20	1.45604E-19	1.62238E-17	1.83675E-19
20			3.80969E-19	3.58108E-19	5.42073E-20	8.8799E-20	1.34353E-17	1.41524E-19
25			2.77472E-19	2.21728E-19			1.11393E-17	1.10491E-19
30			2.05236E-19	1.82016E-19			9.50434E-18	1.14875E-19

Confining Stress (MPa)	Permeability (m^2)							
	10_1	10_3	11_1	11_3	11_4	12_2	12_3	14_1
5	6.8643E-18	3.90911E-18	6.17336E-18	8.40169E-18	6.20851E-18	5.47155E-18	5.19205E-18	1.83636E-16
10	5.87443E-18	3.21462E-18	4.92827E-18	6.78858E-18	5.1806E-18	3.26961E-18	2.98925E-18	1.748E-16
15	5.13486E-18	2.68175E-18	4.23552E-18	5.47805E-18	4.75956E-18	2.82269E-18	2.26781E-18	1.75744E-16
20	4.52835E-18	2.25786E-18	3.91917E-18	4.85592E-18	4.45978E-18	2.26398E-18	1.86253E-18	1.79276E-16
25	4.23812E-18	1.99633E-18	3.42767E-18	4.22775E-18	4.20198E-18	1.95839E-18	1.52654E-18	1.72133E-16
30	3.80334E-18	1.91554E-18	3.34289E-18	4.13754E-18	4.20661E-18	1.74373E-18	1.36656E-18	1.7042E-16

Confining Stress (MPa)	Permeability (m^2)							
	14_2	14_4	16_1	16_3	27_4.2_1	27_4.2_3	30_21.4_4	30_21.4_6
5	2.40314E-16	2.48114E-16	2.26291E-18	2.66886E-18	3.6409E-19	3.85005E-19	4.9922E-19	7.91965E-19
10	2.42174E-16	2.50781E-16	5.55466E-19	6.95038E-19	3.14897E-19	3.02013E-19	4.42982E-19	5.06887E-19
15	2.41168E-16	2.38793E-16	1.85356E-19	3.31706E-19	2.7048E-19	2.22046E-19	3.32399E-19	4.57923E-19
20	2.38218E-16	2.40572E-16			2.05999E-19	1.91999E-19	2.6427E-19	4.3456E-19
25	2.36066E-16	2.3915E-16			1.92803E-19	1.69378E-19	2.45685E-19	3.65291E-19
30	2.3613E-16	2.39076E-16			1.91065E-19	1.61137E-19	2.45305E-19	3.01548E-19

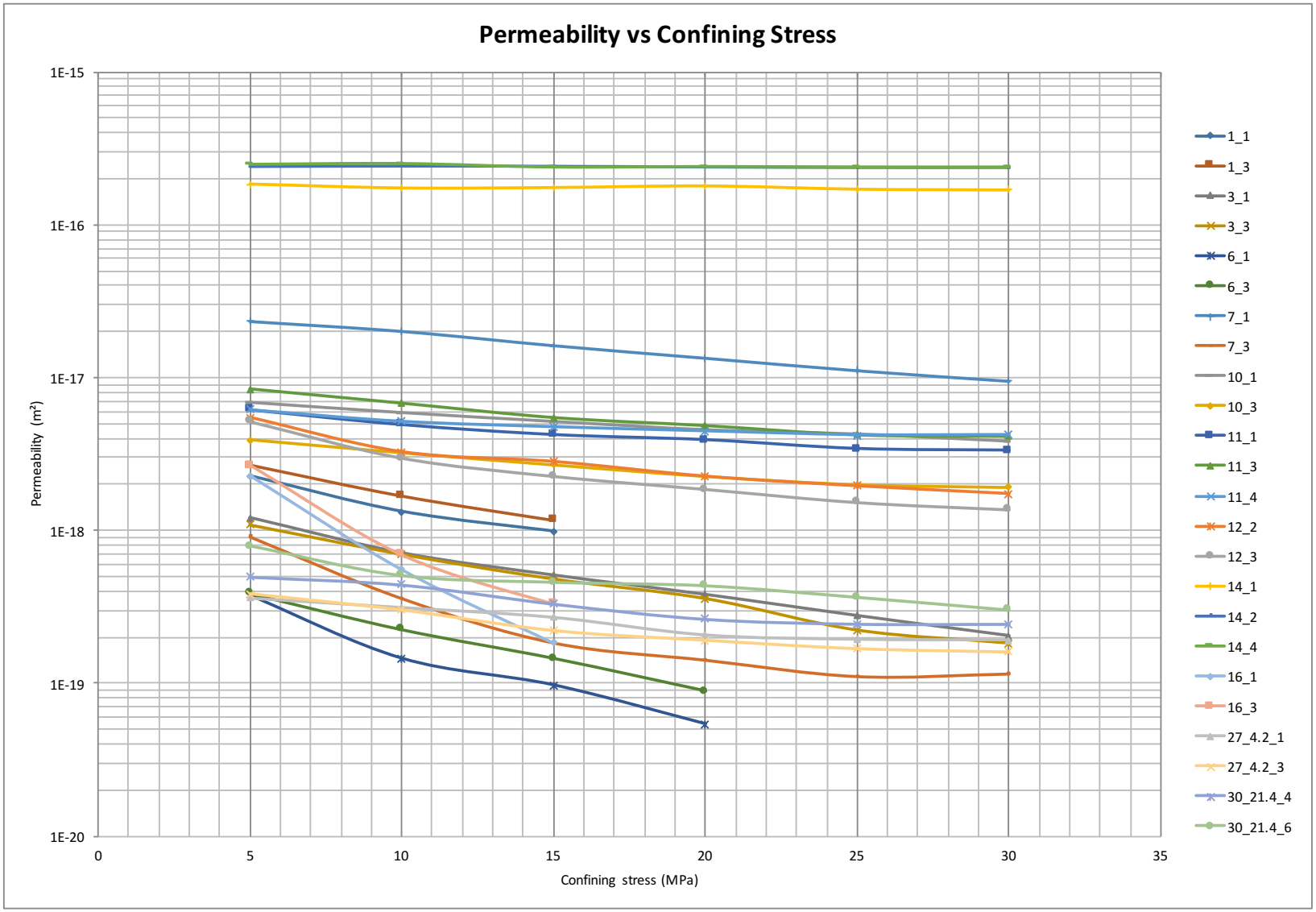

Figure 3.3: Permeability plotted against confining stress for each sample

A key correlation to note is permeability plotted against porosity and density. The best correlation coefficient was achieved when a power law function was fitted; permeability increase has a moderate correlation with an increase in porosity (Figure 3.4). There is a moderate correlation between permeability increase and a decrease in dry density. For consistency, the permeability values for this plot are those tested when a 5 MPa confining stress was applied.

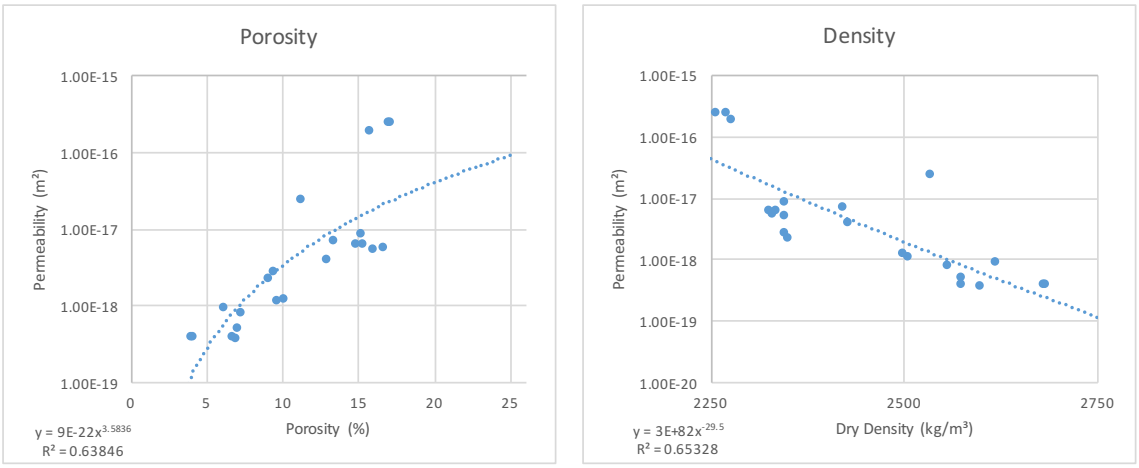

Figure 3.4: Permeability plotted against porosity and density.

3.6 Ultrasonic wave velocity testing

Ultrasonic wave velocity testing was carried out on all but two samples (1_1 and 11_3) which broke during extraction from the permeameter. Table 3.6 presents the average results for each set, along with calculated Young's Modulus and Poisson's ratio.

Table 3.6: Average ultrasonic wave velocity data, Poisson's Ratio and Young's Modulus

Sample Set	P-wave (m/s)	S-wave (m/s)	Poisson's Ratio	Young's Modulus (GPa)
1	4722	2529	0.30	38.9
3	4774	2347	0.34	37.1
6	4878	2709	0.28	50.3
7	4489	2476	0.28	40.4
10	4545	2428	0.30	37.2
11	4101	2679	0.13	37.7
12	4387	2201	0.33	30.4
13	4533	2553	0.27	46.4
14	4225	2384	0.27	32.8
15	2682	1573	0.24	11.7
16	4024	2143	0.30	23.6
27_4.2	4443	2603	0.24	43.5
30_21.4	4054	2514	0.19	38.7

Key data relationships to plot against ultrasonic wave velocities are density, porosity and permeability. These datasets are plotted in Figures 3.5, 3.6 and 3.7. The unreliable porosity and density values have been removed for their corresponding plots. The correlation of each plot is outlined in Table 3.7.

Table 3.7: Correlation between ultrasonic waves and density, porosity and permeability.

		Parameter		
		Density	Porosity	Permeability
P-Wave Velocity	Correlation	Positive	Negative	Negative
	Strength	Moderate	Moderate	Weak
S-Wave Velocity	Correlation	Positive	Negative	Negative
	Strength	Moderate	Moderate	Weak
Poisson's Ratio	Correlation	None	None	None
	Strength	None	None	None
Young's Modulus	Correlation	Positive	Negative	Negative
	Strength	Strong	Moderate	Moderate

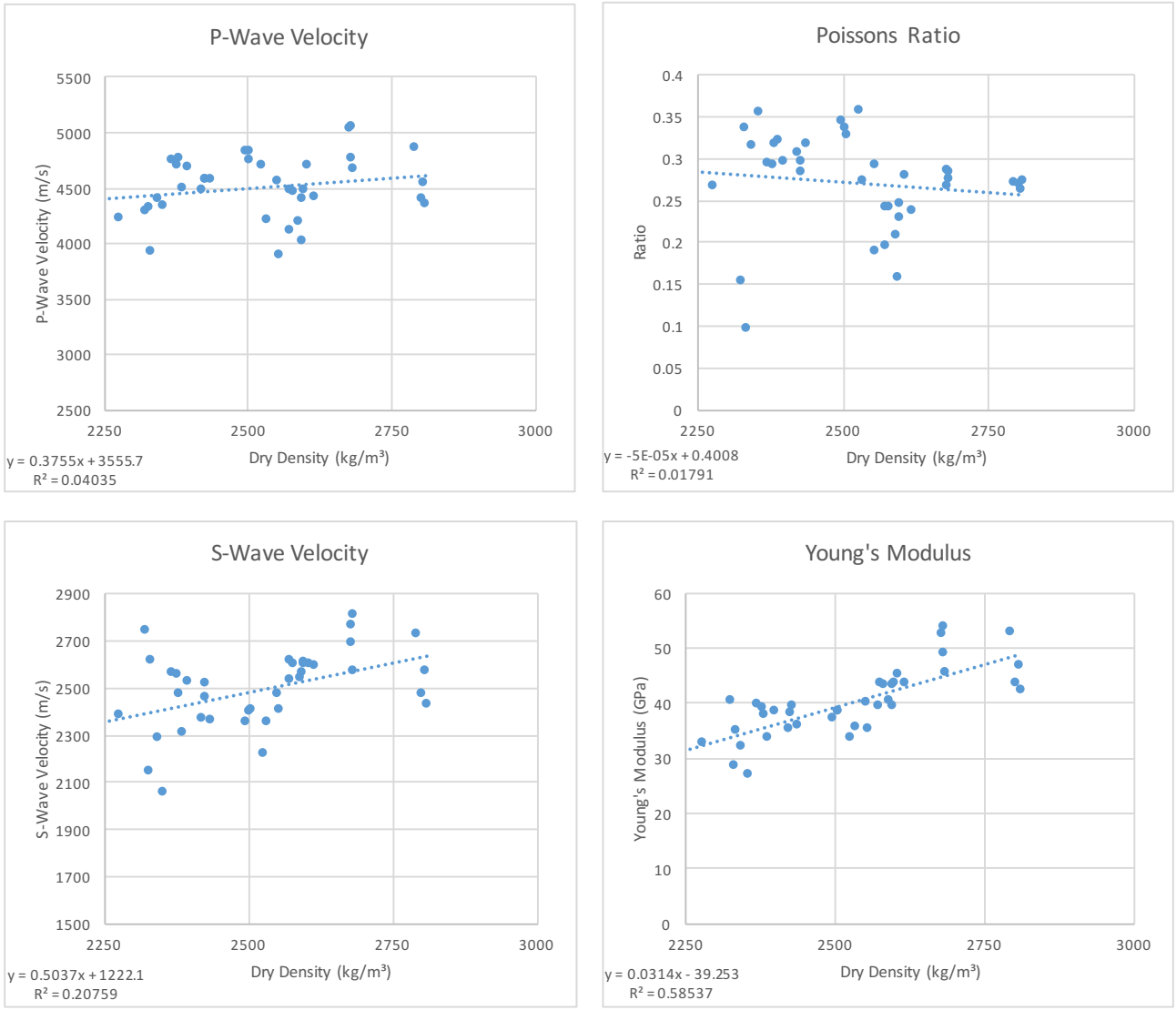

Figure 3.5: Density plotted against ultrasonic wave velocities, Young's Modulus and Poisson's Ratio

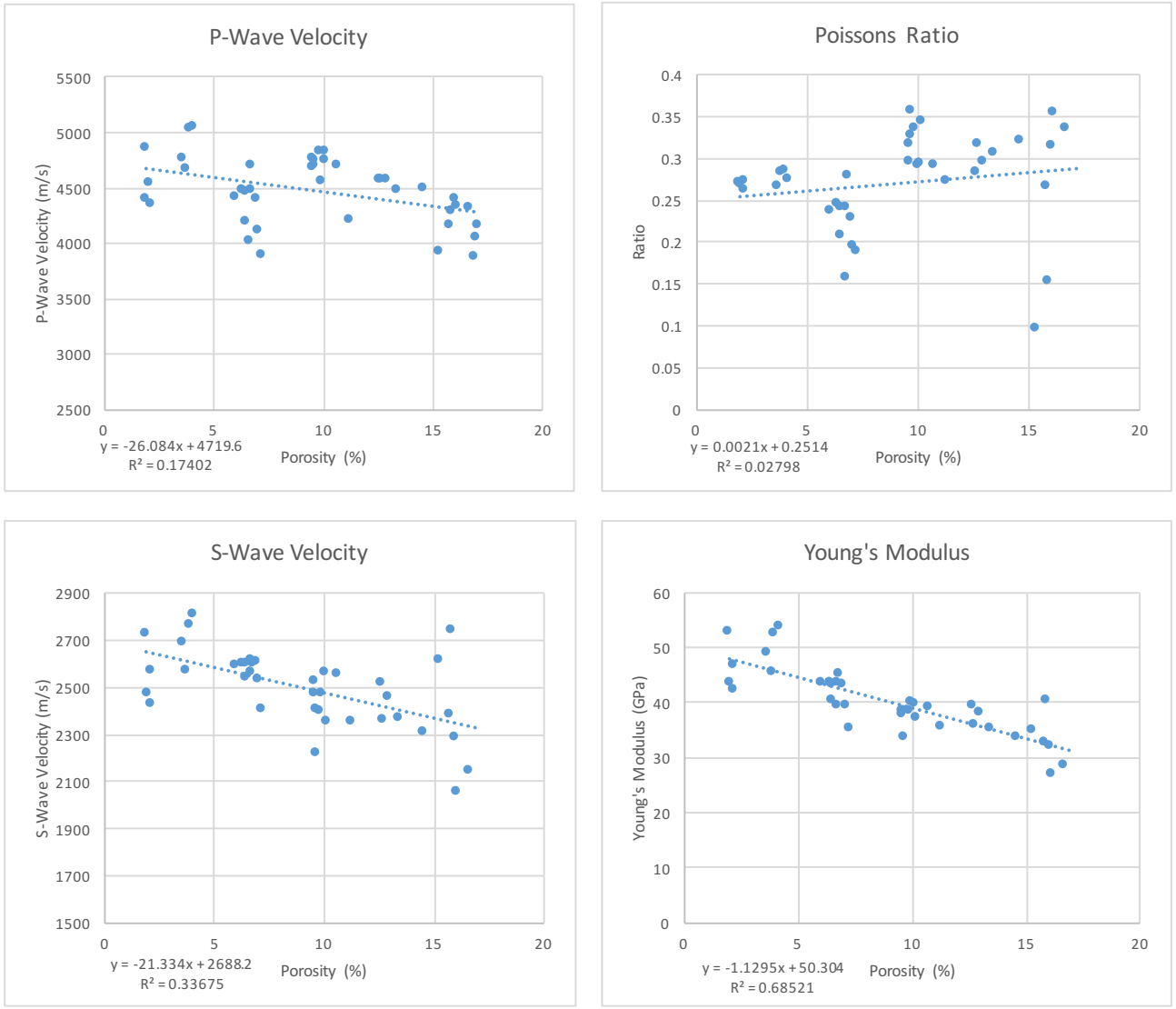

Figure 3.6: Porosity plotted against ultrasonic wave velocities, Young's Modulus and Poisson's Ratio

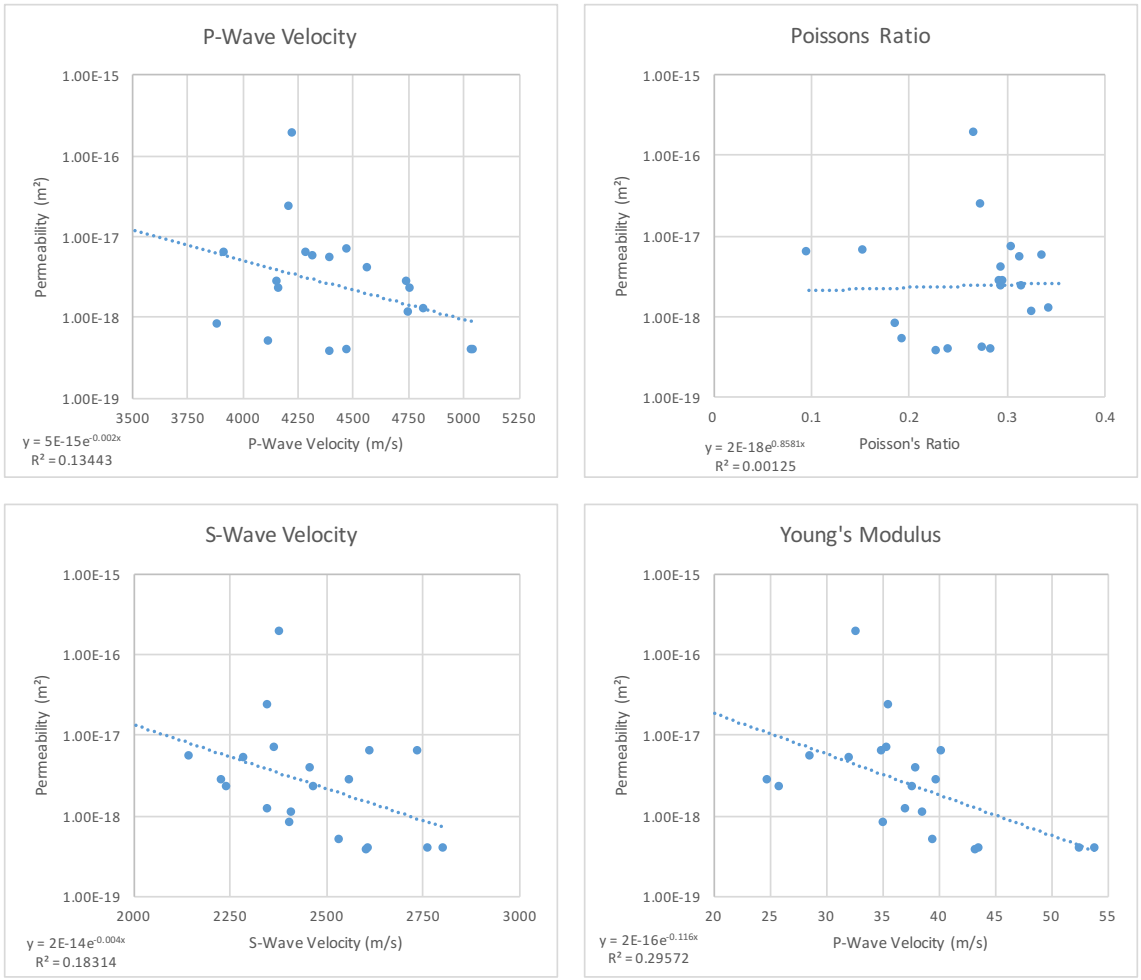

Figure 3.7: Permeability plotted against ultrasonic wave velocities, Young's Modulus and Poisson's Ratio

3.7 Triaxial testing

The stress-strain relationship for the triaxial testing of samples 11 and 14 at different effective pressures. (Figure 3.8) shows that only sample 11 at 40 MPa effective pressure has a sharp stress drop with increasing strain. The 14 sample at the same effective pressure has a slight stress drop at greater than 4% strain. Both samples show gradual strain softening at 70 MPa confining stress.

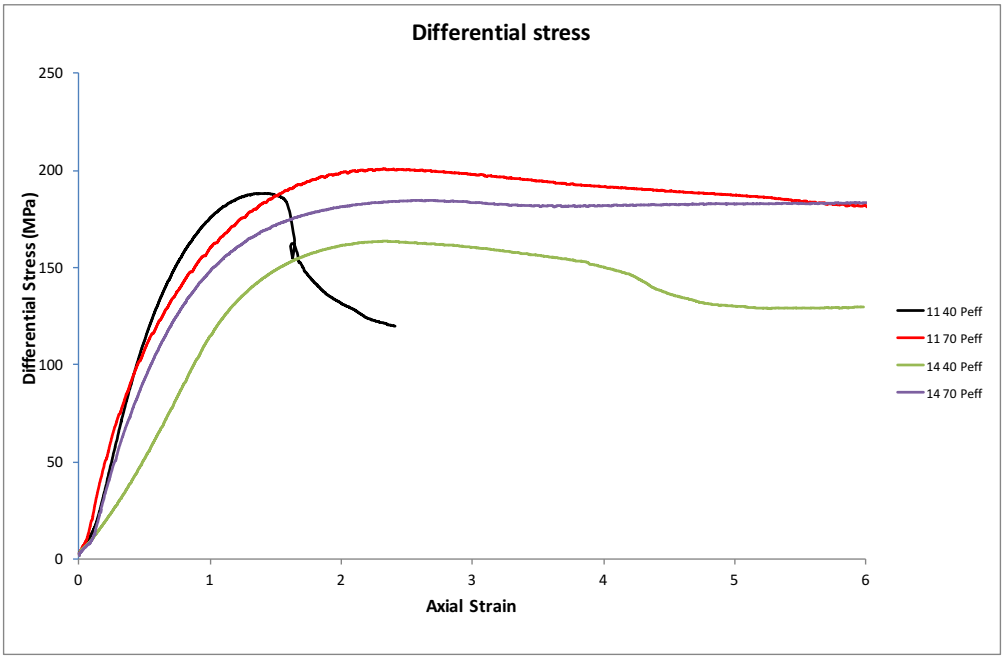

Figure 3.8: Differential stress plotted against axial strain for two samples of 11 and 14 at varying effective pressure (40 MPa and 70 MPa)

Porosity reduction (compaction) occurs at low strain for all samples, but is reversed (dilation) with increasing micro fracturing (during straining) in all but the 14 sample at 70 MPa confining stress (Figure 3.9). This particular sample has undergone compaction throughout the entire test up to 6% strain.

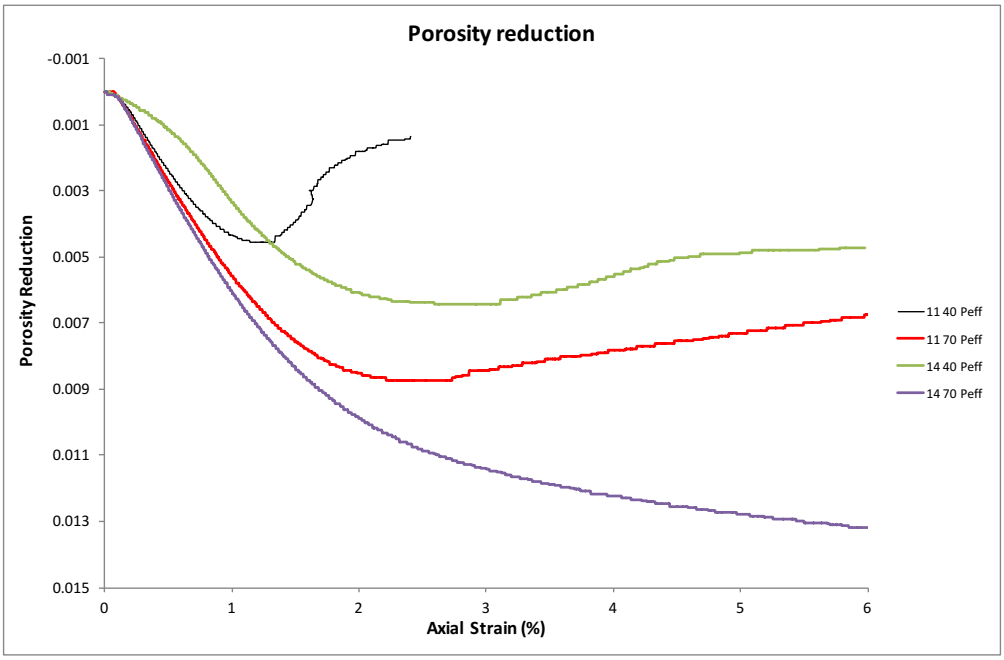

Figure 3.9: Porosity reduction plotted against axial strain for two samples of 11 and 14 at varying effective pressure (40 MPa and 70 MPa)

Chapter 4

Discussion

4.1 Introduction

One of the most important properties in a geothermal system is permeability. Matrix permeability (i.e. intact rock permeability) is controlled by the overall morphology and microstructure of a rock sample. The morphology and microstructure are a result of the composition, mode of emplacement and any subsequent geological events occurring after emplacement (Cant, 2015).

Geothermal environments, including the Rotokawa Geothermal Field, are typically situated in geochemically harsh, volcanically and tectonically active areas, creating highly altered, microstructurally complex and spatially variable rocks. This highlights that while geological units may be grouped, significant variation exists within them.

Siratovich et al. (2014) showed that Rotokawa Andesite contains a pervasive network of isotropic microcracks induced by thermal stress. Multiple episodes, including initial eruption, burial in a faulted graben, hydrothermal alteration and exhumation during core recovery, have caused the rocks to undergo multiple heat and cooling cycles (Rae, 2007; Siratovich et al., 2014).

Siratovich et al. (2014) demonstrated the extent of micro-fracturing was a significant factor in the other measured physical and mechanical properties, such as ultrasonic wave velocities and uniaxial strength. Similar conclusions have been presented by multiple authors (e.g. Vinciguerra et al., 2005; Keshavarz et al., 2010).

In this chapter, physical property relationships are investigated, in particular how they relate to the matrix permeability. This is followed by a discussion of how these relationships can be of use to geothermal exploitation and other applications.

4.2 Matrix permeability and connected porosity relationship

It is a logical assumption that permeability correlates with porosity, whereby the connected pore space provides a pathway for fluid migration (Siratovich, 2014). However, an understanding of the physical nature (i.e. connectivity and tortuosity) of this connected porosity is required to fully understand and determine what physical properties control this relationship. Because density and porosity are closely related (i.e. a more porous rock is less dense, Figure 3.1), and the pore space is critical for fluid transport, investigation is concentrated on porosity.

Overall, a clear trend can be observed of increasing porosity with increasing permeability, demonstrated by Plot A in Figure 3.4. This same relationship has been observed by several authors (e.g. Stimac et al., 2004; Cant, 2015; Siratovich et al., 2014; Bourbie and Zinszner, 1985). In line with these papers, a power law function was the best fit to the data with comparable correlation coefficient of 0.65. There were two outliers; sample 7_1 (suspected equipment error) and sample set 14 (investigated below). When the outliers were removed, the correlation coefficient increased to 0.84 (Figure 4.1).

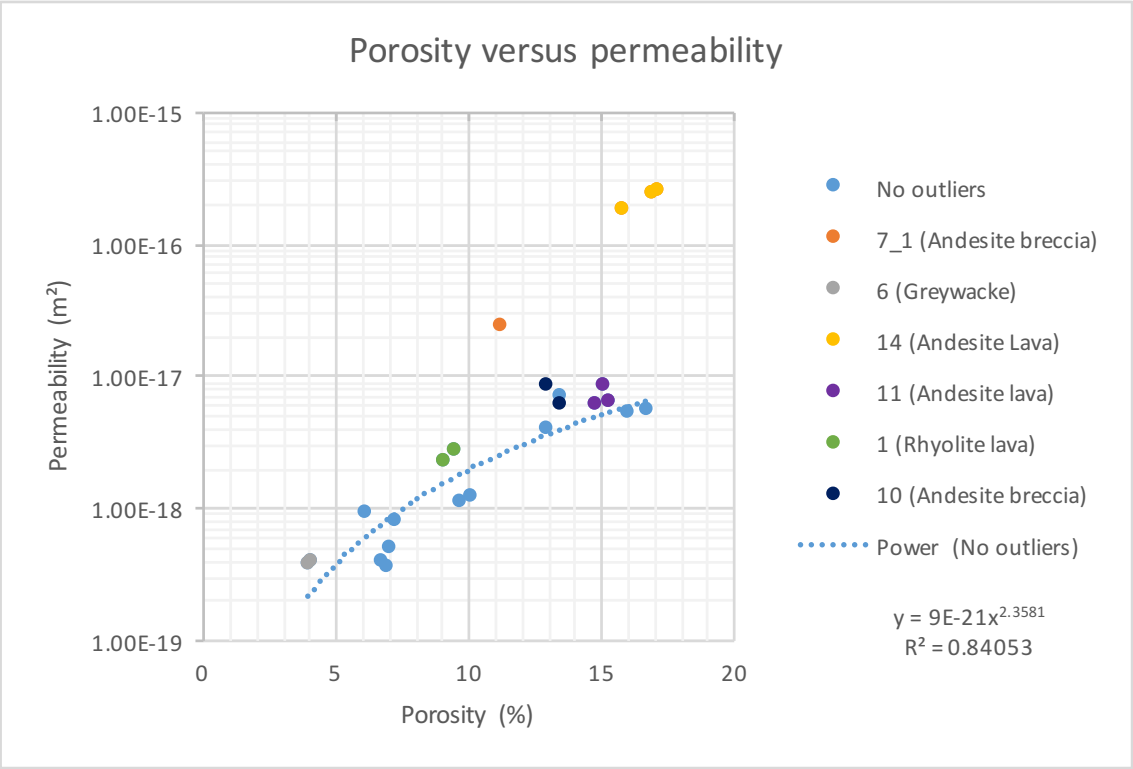

Figure 4.1: Permeabilty plotted against connected porosity. Power law correlation fitted with outliers 7_1 and 14 removed.

Heap et al. (2014b) found when fitting a power law trend to the porosity permeability relationship for andesites from Volcán de Colima, Mexico, that there were two distinct families; low porosity (7 to 12%) and high porosity (15-24%). At RGF, most data falls on a single best fit line.

4.2.1 Microstructural control

Matrix permeability is not only controlled by pore volume, but also the morphology and pore space microstructure of each rock (Cant, 2015), resulting in the moderate data scatter in Figure 4.1. The measurement of connected porosity is independent of time, so ignores the microstructure of the porosity. Regardless of how complex the connected porosity is, given enough time, all connected porosity will be accounted for. Permeability, however is dependent on time, where samples with similar porosity can have significantly different permeabilities if the connected porosity of one is more tortuous than the other.

Siratovich et al. (2014) used SEM analysis and Cant (2015) created binary photomicrograph maps using a fluorescent light microscope to examine microstructure. The

SEM imaging captured pore shape and microfractures with better clarity and contrast than the fluorescent images. Therefore, the decision was made to use the SEM for this research.

Using the electron back scatter detector, the SEM produces images which contrast atomic weight, therefore, black pixels illustrate low atomic weight suggesting pore or fracture space and lighter pixels illustrate rock mass.

Figure 4.2 shows the microstructure of thin sections 11 and 14. These sample sets have porosity within 2% of one another, yet permeability is nearly two orders of magnitude different (Table 3.4).

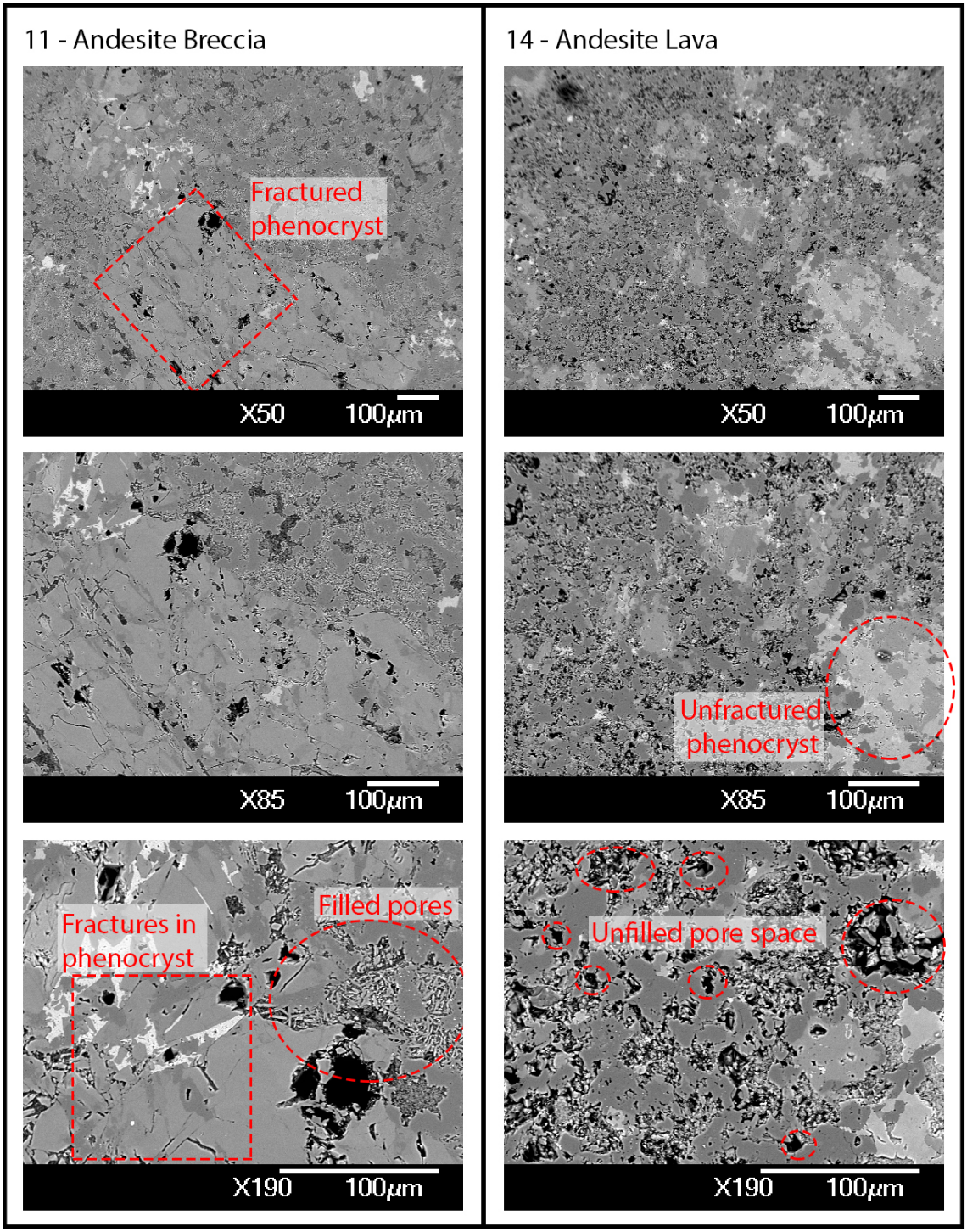

Figure 4.2: SEM images highlighting the microstructure contrast between thin sections 11 and 14.

In thin section 11 (andesite breccia), pores are connected by microfractures which propagate through phenocrysts. The majority of the surrounding groundmass appears to be filled pore space, which which is common for a volcanic breccia. The microfracture network creates a narrow, tortuous path for fluid to flow through, causing the rock to have a lower permeability.

In thin section 14 (andesite lava) micro-fracturing appears to be non-existent. The majority of the pore space is unfilled and connection of pores promotes easier fluid flow through the sample, resulting in the higher permeability. The pore space in 14 is more evenly distributed than in 11, encouraging the connectivity throughout the thin section, further promoting the higher permeability.

Figure 4.3 presents sample images from thin sections 1, 6 and 10. All of these three sample sets fit the trend line. Thin section 1 (rhyolite lava) shows a similar structure to thin section 11, whereby a microfracture network exists within phenocrysts. The micro-fracturing is less prominent causing fewer pathways for fluid to travel. This combined with lower porosity has caused the permeability to be lower than sample set 11.

Fracturing within thin section 10 (andesite breccia) appears to be through the matrix. The fracture presented in Figure 4.3 for thin section 10 does not appear to extend across the image, suggesting fracturing is localised and stress induced. The groundmass is similar to sample set 11, and the porosity and permeability is slightly less.

The splintering shown in thin section 6 was likely to be mechanically induced during the polishing of the thin section, suggested by the presence of fine grained fragments within the crack, the width of the crack aperature and the difference to historic infilled cracks. The semi metamorphosed fine groundmass with very few pores gives the sample very low porosity, and in turn a low permeability.

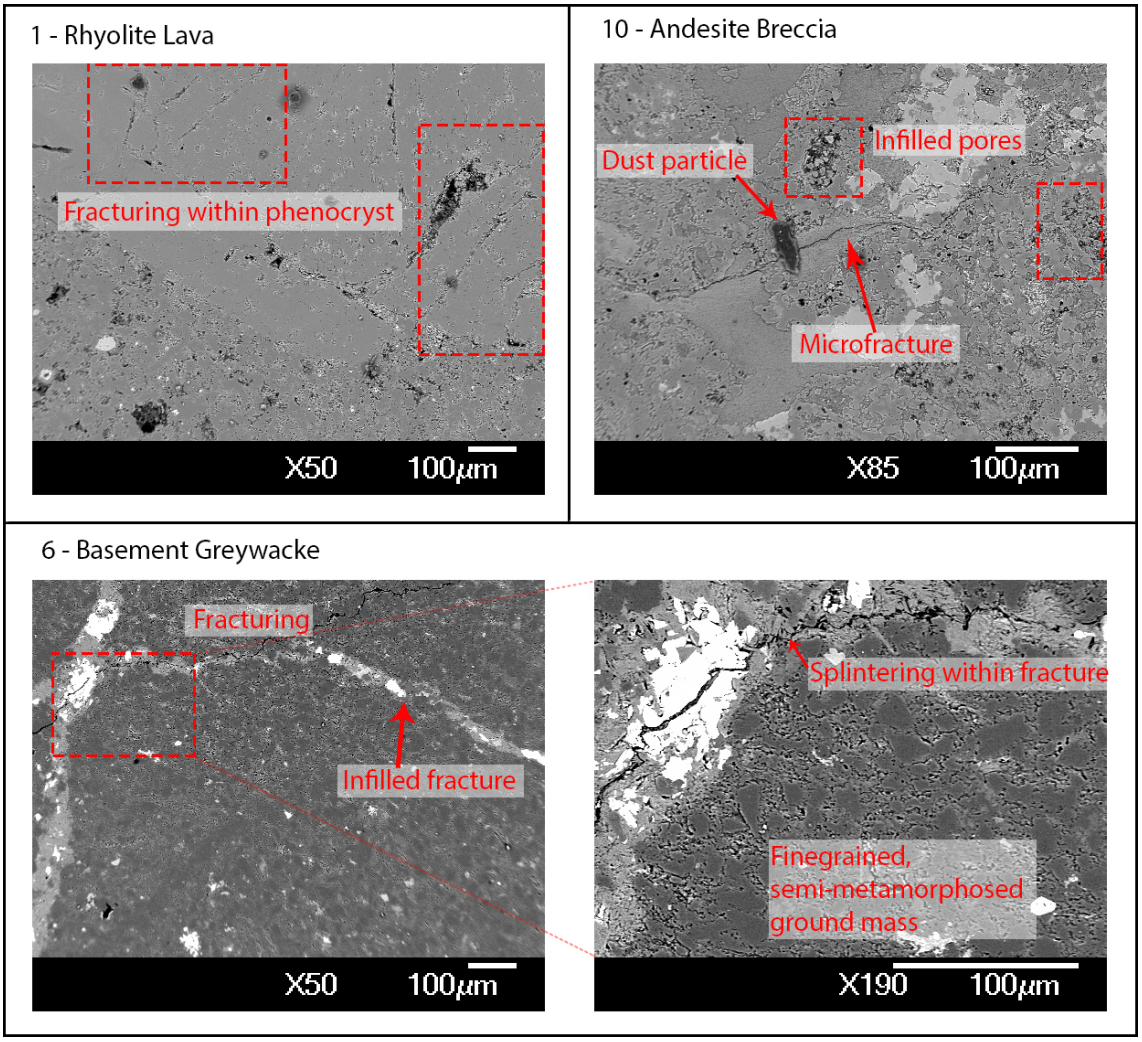

Figure 4.3: SEM images highlighting the microstructure of thin sections 1 (rhyolite lava), 6 (hydrothermally altered greywacke) and 10 (andesite breccia).

4.2.2 Triaxial testing

Two samples from each of sets 11 and 14 were tested at 40 MPa and 70 MPa effective pressure using a triaxial testing rig at the Université de Strasbourg, France (Figures 3.8 and 3.9).

As described in the SEM analysis, thin section 11 has a network of pre-existing micro-fractures and cracks. Initially at 40 MPa confinement, crack closure is followed by a period of new cracks forming, until ultimately, post peak brittle failure (Figure 3.8). The pre-existing fractures highlight that this sample is brittle and has a tendency to create new fractures. Because the pores are in-filled, they are difficult to close up,

causing the porosity reduction to decrease as new fractures open. At 70 MPa, the increased confinement causes the pre-existing fractures to be more closed, making it harder to generate new fractures and open them.

The SEM images of sample 14 display open pore space and no pre-existing fractures. This suggests the rock is less brittle, which in turn means it is more difficult to generate new fractures. Because the pores are free of infilling, the pores are easier to close up, as demonstrated by the porosity reduction plots (Figure 3.9). During deformation, the pores are closing causing the constant porosity reduction, in particular at 70 MPa confinement, where it appears porosity reduction will continue with additional deformation.

The triaxial testing was carried out at higher effective pressure than those calculated for reservoir conditions, however, the results highlight the mechanical controls and how variable the strength can be for two samples of Rotokawa Andesite, even with similar porosity.

It must be noted that these triaxial tests were carried out at ambient temperature, removing any effect temperature has on each sample when triaxial loading. Heap et al. (2014a) showed increasing the temperature from ambient to 750°C halved the porosity reduction at 50 MPa effective pressure, for the Neapolitan Yellow Tuff. This highlights that temperature may have an influence on rocks, but to determine the extent, testing on the Rotokawa Andesite samples at temperature would have to be conducted.

4.2.3 Ultrasonic wave velocities

There is a very weak correlation between increasing porosity and decreasing P and S wave velocities (Plot A of Figure 4.4). This trend, although weak, has been observed by multiple authors (e.g. Siratovich et al., 2014; Wyering et al., 2014; Cant, 2015). Siratovich et al. (2014) observed similar levels of variation and wide spread distribution, and suggested the cause of this scatter may be attributed to the nature of the connected porosity. The presence and distribution of pores in each of the samples effects the propagation of P and S waves.

The correlation between permeability and P and S waves is even weaker than for porosity, and caution should be used if attempting to use P and S wave velocities in the field to predict permeability.

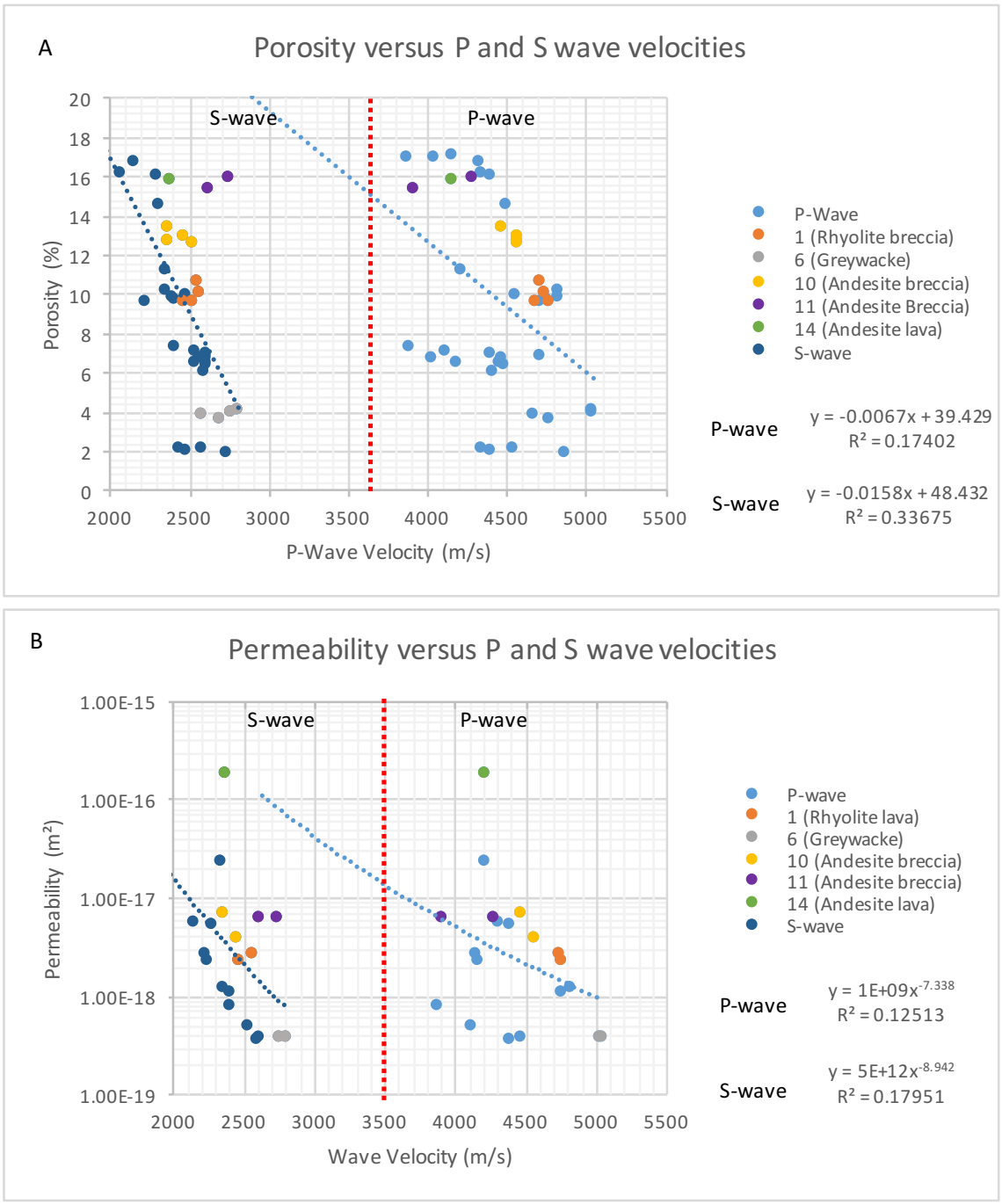

Figure 4.4: Ultrasonic wave velocities plotted against porosity and permeability (at 5 MPa).

4.3 Effect of confining stress

Increasing the confining stress of samples in a laboratory can be used as a proxy for increased depth. This provides empirical data to relate to the mechanical processes occurring to these rocks at varying depth in a geothermal reservoir.

As observed in Figure 3.3, increasing confining stress causes a decrease in permeability for most samples.

It is suggested in Cant (2015), the nature of connected porosity and the extent of fracturing within samples plays a significant role as to how sensitive rocks are when an effective stress is applied. Cant (2015) found that samples which had predominantly microfracture porosity were much more sensitive to confining stress, as seen by a larger decrease in permeability when confining stress was applied. Samples that had vesicular porosity exhibited minimal change when confining stress was applied. Elastic deformation controls closure of cracks, with surface roughness controlling further closure (Cant, 2015). Closure of vesicles requires much larger effective confining stress, and would ultimately lead to irreversible pore collapse, resulting in drastic reduction of permeability (Roegiers, 1995).

This same conclusion can be presented for this dataset by contrasting sample sets 11 and 14. As explained in Section 4.2.1, the microstructure of thin section 11 has a dominant fracture network through its phenocrysts, whereas thin section 14 exhibits vesicular porosity. Figure 4.5 highlights the permeability versus increased confining stress for these two sample sets, along with sample set 16.

The vesicle dominated sample set 14 does not decrease in permeability, even when 30 MPa is applied. In comparison, the permeability of the fracture dominated sample set 11 progressively reduces up to half its original permeability at 30 MPa confinement.

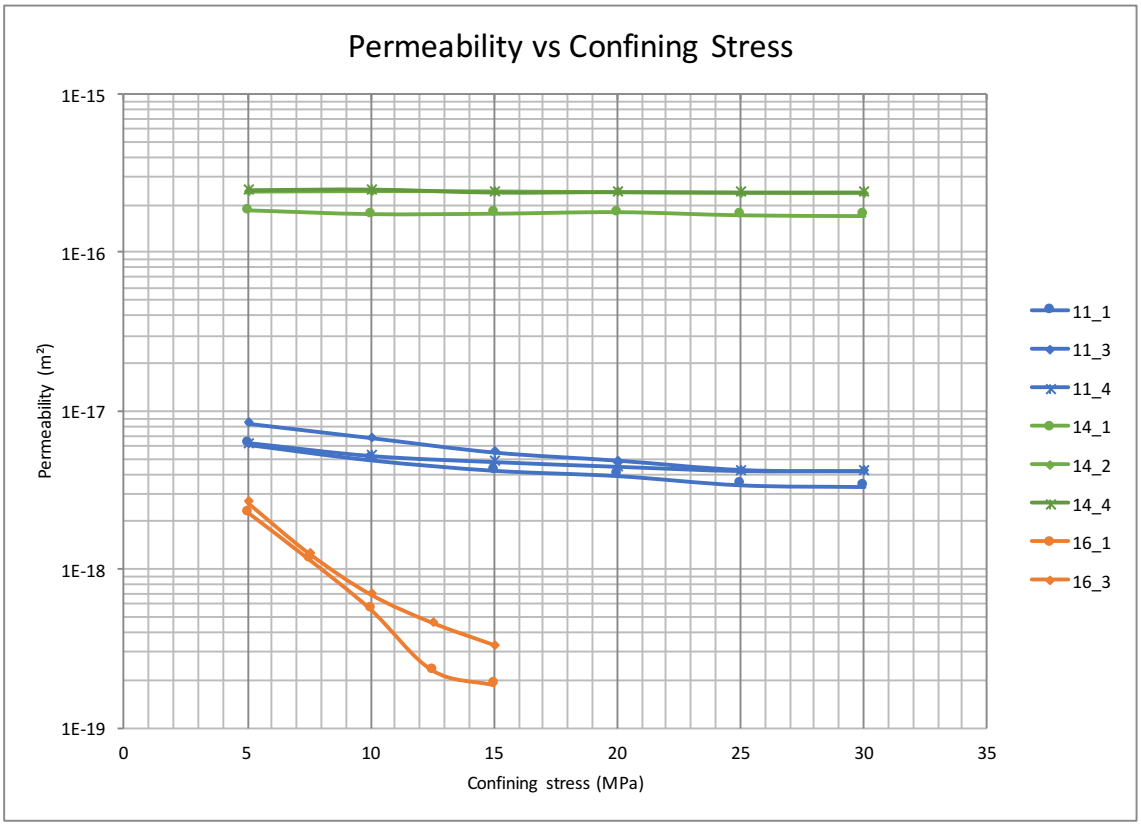

Figure 4.5: Permeability versus confining stress for sample sets 11, 14 and 16

Sample set 16 (rhyolite breccia) was included in Figure 4.5 because it exhibited the highest sensitivity to confining stress. The confinement was only increased to 15 MPa for this sample set because the calculated in situ stress was determined to be very low (5 MPa). Nevertheless, the permeability nearly decreased an order of magnitude. It was expected that this sample would contain a significant fracture network within it, causing elastic closure of these fractures restricting flow through the sample. There are no SEM images for this sample, but an example from the petrographic thin section analysis (Figure 4.6) shows pervasive fractured phenocrysts.

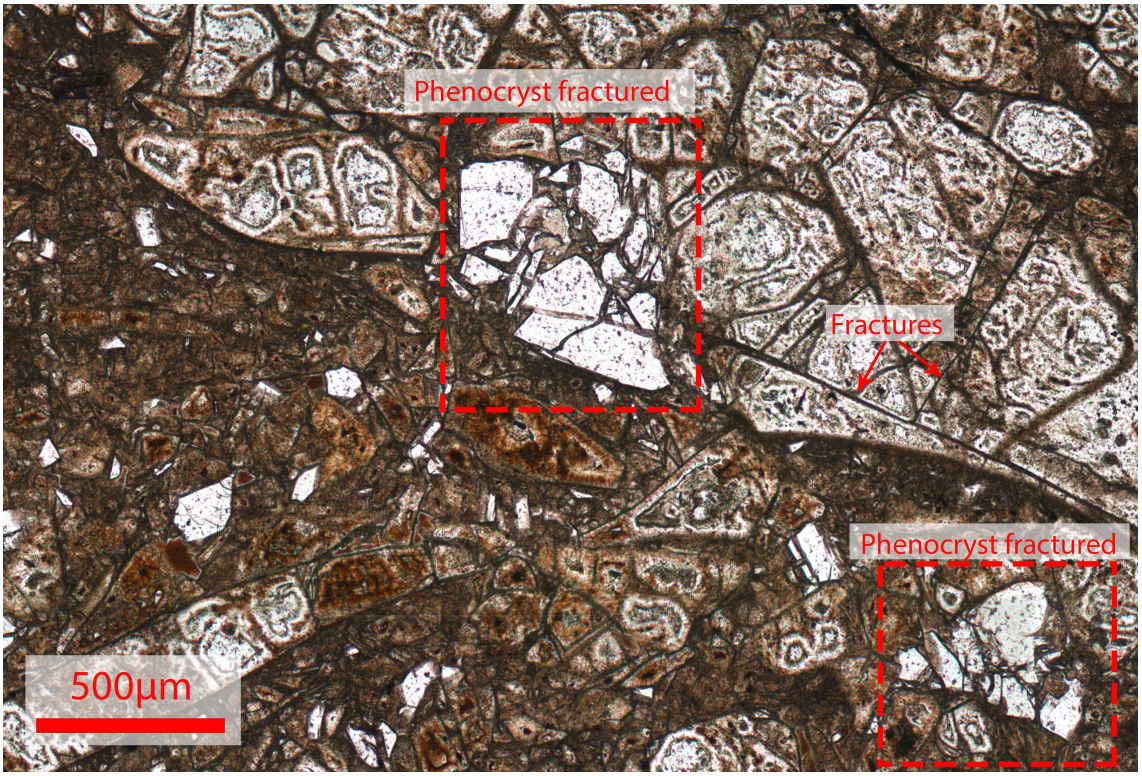

Figure 4.6: Thin section image for sample set 16 highlighting fracturing within the sample. Plane polarised light.

4.4 In situ permeability

A critical application of this data is to determine in situ permeability values. To determine an estimate of the in situ permeability for each sample, the lithostatic model can be applied. Table 4.1 provides a summary of the calculated in situ stress values from the lithostatic model for each sample, along with the calculated permeability value from the permeameter test run at the closest confining stress.

Table 4.1: In situ confining stress calculated from the lithostatic model with the closest tested confining stress and the corresponding permeability.

Sample	Rock	Type	Well	Depth (m)	Calculated in situ stress (MPa)	Tested confining stress (MPa)	Permeability (m^2)
16_1	Rhyolite	Breccia	34	501	5.0	5	2.26E-18
16_3	Rhyolite	Breccia	34	501	5.0	5	2.67E-18
1_1	Rhyolite	Lava	9	905	12.1	12.5	1.09E-18
1_3	Rhyolite	Lava	9	905	12.1	12.5	1.24E-18
3_1	Greywacke	Conglomerate	9	1747	22.6	25	2.77E-19
3_3	Greywacke	Conglomerate	9	1747	22.6	25	2.22E-19
7_3	Andesite	Breccia	24	1821	30.2	30	1.15E-19
11_1	Andesite	Breccia	27	1852	25.2	25	3.43E-18
11_3	Andesite	Breccia	27	1852	25.2	25	4.23E-18
11_4	Andesite	Breccia	27	1852	25.2	25	4.20E-18
12_2	Andesite	Lava	27	1854	25.2	25	1.96E-18
12_3	Andesite	Lava	27	1854	25.2	25	1.53E-18
27_4.2_1	Andesite	Lava	27	2120	31.6	30	1.91E-19
27_4.2_3	Andesite	Lava	27	2120	31.6	30	1.61E-19
10_1	Andesite	Breccia	25	2200	30.3	30	3.80E-18
10_3	Andesite	Breccia	25	2200	30.3	30	1.92E-18
30_21.4_4	Andesite	Lava	30	2320	28.7	30	2.45E-19
30_21.4_6	Andesite	Lava	30	2320	28.7	30	3.02E-19
6_1	Greywacke	Sandstone	20	2606	38.0	20	5.42E-20
6_3	Greywacke	Sandstone	20	2606	38.0	20	8.88E-20

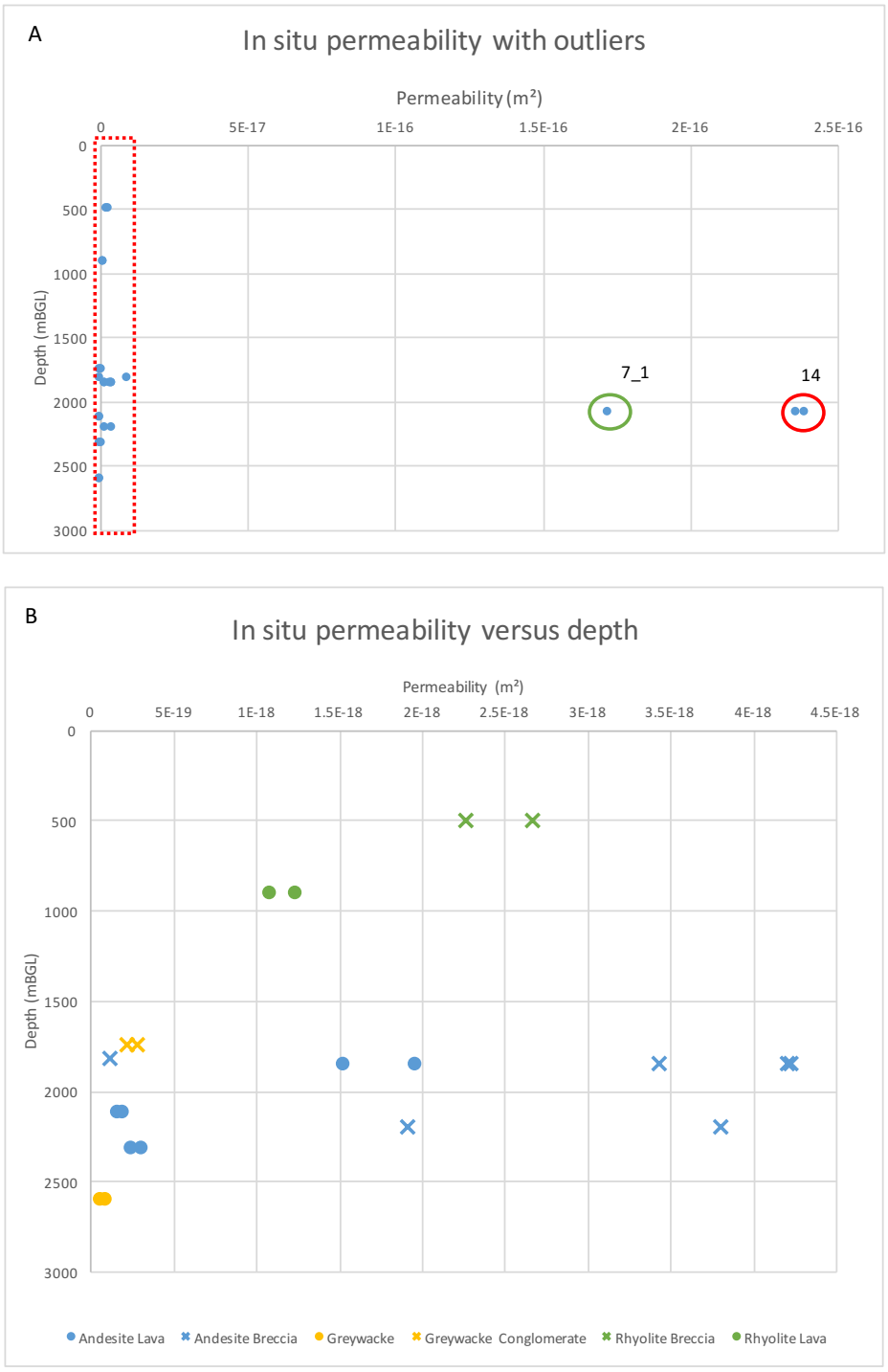

Figure 4.7: Plot A: In situ permeability plot of all data. Outliers 7_1 and set 14 are highlighted. Plot B: In situ permeability plot of area outlined in the dotted red box in Plot A (outliers removed).

As seen in Figure 4.7, there is no distinct correlation between in situ permeability and depth. Cant (2015) observed a similar result, where a lithological correction was applied, to identify clusters of similar behaviour for each rock type.

In plot B in Figure 4.7, outliers were removed and the data was colour coded in relation to rock type to identify any clusters, but it appears none exist. There is a wide range of permeabilities for the andesite lava and breccia. The colours are banded laterally, in particular the andesite samples, but this is solely a depth observation, which corresponds to the lithology.

The lack of correlation is once again related to the microstructure of each sample, and how each rock responds differently to increased confining stress. In particular, the Rotokawa Andesite, which varies laterally and vertically, and is the result of several eruptive flows (McNamara et al., 2015). The Rotokawa Andesite is not grouped on its mechanical and physical properties, which have been shown to be variable, but rather it forms a geochemically coherent group (McNamara et al., 2015).

Based on testing of bore-hole samples from Campi Flegrei volcanic area (Italy), Heap et al. (2014a) showed the relationship between porosity and permeability in regards to depth was variable, demonstrating that there is no simple relationship between depth and mechanical compaction, chemical alteration, porosity and permeability.

4.5 Application to geothermal exploration and exploitation

The purpose of conducting this research is the ability to use some of the relationships to help predict hard to obtain parameters, such as permeability, during the exploitation of geothermal systems. The core used in this study was extremely expensive, time consuming and potentially risky to recover (Siratovich, 2014; Hole, 2013).

There are downhole geophysical logging techniques for measuring porosity and ultrasonic wave velocity measurements (Siratovich et al., 2014). With the use of the relationships described in this thesis, these measurements (in particular porosity) can be used to predict values which are more difficult to obtain, such as permeability.

It must be emphasised that these predictions are only estimates. The scatter of data, caused by the heterogeneous nature of the geology, results in some rocks behaving differently than expected. A prime example of this is the similarities and differences between samples 11 (breccia) and 14 (lava) from the Rotokawa Andesite unit. Another example is the very poor fit of ultrasonic wave velocities with permeability.

The Rotokawa Andesite is grouped based on a geochemical signature (McNamara

et al., 2015), and not on physical and mechanical properties. From a rock mechanics perspective, the variability in the mechanical relationships described in this thesis demonstrate the importance of thorough investigation of localised samples, especially when hosted in a hydrothermally active system.

Siratovich et al. (2014) fitted microstructural and empirical correlations which took into account micro-structural variances in the model. The use of the data in this thesis could be used to further refine these models.

Shale gas reserves often have economical flow rates down to the nano-Darcy range (1nD = $9.87e^{-22}$ m^2; Ghanizadeh et al., 2013), which is comparable to the data collected in this thesis. Although shale gas is hosted in sedimentary rocks, the fundamental understanding of fluid flow controls presented in this thesis can help with the poor understanding of the processes involved in fluid transport within the fracture and matrix systems of these lithotypes (Ghanizadeh et al., 2013).

4.6 Further research

Fractures would seem to control how sensitive rocks are to increasing confining stress, as suggested by various authors (e.g. Siratovich et al., 2014; Cant, 2015), and presented in Section 4.3. In this study, intact rock was used, and physical properties controlling the behaviour of these rocks were investigated on a microscopic scale. Further research as to how significant the decrease in permeability is in larger macroscopic scale fractures would be beneficial. Contrasting this with the matrix permeability would help to determine the significance of matrix permeability at depth, especially in samples such as 14, where confining stress up to 30 MPa resulted in no decrease in permeability.

Although the ultrasonic wave velocity data provided poor correlation with other parameters, further testing would be beneficial. The testing in this study was carried out with minimal (1 MPa) confining stress. Determining the effect confining stress has on wave velocities would provide data to relate to these measurements at depth. Fortin et al. (2011) observed an increase wave velocity with an increase in confining stress, confirming the closure of micro-fractures. Measuring ultrasonic wave velocities under confinement could provide a better fit to in situ permeability.

Chapter 5

Conclusions

The objective of this thesis was to carry out a systematic laboratory study of the physical and mechanical properties of the Rotokawa Geothermal Field and relate them to in situ stress conditions. The following are key conclusions of the thesis:

- There is a clear relationship between increasing connected porosity and increasing permeability, fitted with a power-law function. The presence of outliers demonstrates the significance of microstructure on the porosity-permeability relationship, where rocks with similar porosities, can have significantly different permeabilities.
- Microstructure controls the behaviour of samples during triaxial testing. The presence of pre-existing fractures relates to brittle failure, where new fractures are easier to generate. Lack of pre-existing fractures and the presence of open pore space promotes pore collapse and no fracture generation.
- Ultrasonic wave velocities have minimal correlation with permeability and porosity, and caution should be used when using these relationships for estimating in situ properties. This testing was carried out unconfined. Confining the samples during testing has the potential to correlate better.
- There is a general trend of increasing confining stress with a decrease in permeability. The presence of microfractures results in more sensitivity to confining stress on permeability. Samples with no microfractures and open pores, show no decrease in permeability with confining stress.
- There is no distinct trend between in situ permeability and depth, nor between permeability and rock type.

- While there is a general relationship between porosity and permeability, the effect of microstructure can cause significant variation, so correlation may be used taking into account a variability within half an order of magnitude.

References

Bibby, H., Caldwell, T., Davey, F., and Webb, T. (1995). Geophysical evidence on the structure of the Taupo Volcanic Zone and its hydrothermal circulation. *Journal of Volcanology and Geothermal Research*, 68(1-3):29–58.

Bourbie, T. and Zinszner, B. (1985). Hydraulic and acoustic properties as a function of porosity in Fontainebleau Sandstone. *Journal of Geophysical Research*, 90(B13):11524–11532.

Bowen, R. (1979). *Geothermal Resources*. Applied Science Publishers, Great Yarmouth, UK.

Bowyer, D. and Holt, R. (2008). Case study: Development of a numerical model by a multi-disciplinary approach, Rotokawa Geothermal Field, New Zealand. In *Proceedings World Geothermal Congress 2010, Bali, Indonesia*, Bali.

Brace, W. F., Walsh, J. B., and Frangos, W. T. (1968). Permeability of granite under high pressure. *Journal of Geophysical Research*, 73(6):2225–2236.

Brown, S. J. a., Wilson, C. J. N., Cole, J. W., and Wooden, J. (1998). The Whakamaru group ignimbrites, Taupo Volcanic Zone, New Zealand: Evidence for reverse tapping of a zoned silicic magmatic system. *Journal of Volcanology and Geothermal Research*, 84(1-2):1–37.

Cant, J. L. (2015). Matrix Permeability of Reservoir Rocks , Ngatamariki Geothermal Field, Taupo Volcanic Zone , New Zealand. *Unpublished MSc thesis, University of Canterbury, Christchurch, New Zealand.*

Cataldi, R., Hodgson, S. F., and Lund, J. W. (1999). *Stories from a Heated Earth.* Geothermal Resources Council and International Geothermal Association.

Cole, J., Deering, C., Burt, R., Sewell, S., Shane, P., and Matthews, N. (2014). Okataina Volcanic Centre, Taupo Volcanic Zone, New Zealand: A review of volcanism and

synchronous pluton development in an active, dominantly silicic caldera system. *Earth-Science Reviews*, 128:1–17.

Deering, C. D., Cole, J. W., and Vogel, T. A. (2011). Extraction of crystal-poor rhyolite from a hornblende-bearing intermediate mush: a case study of the caldera-forming Matahina eruption, Okataina volcanic complex. *Contributions to Mineralogy and Petrology*, 161(1):129–151.

Fortin, J., Stanchits, S., Vinciguerra, S., and Guéguen, Y. (2011). Influence of thermal and mechanical cracks on permeability and elastic wave velocities in a basalt from Mt. Etna volcano subjected to elevated pressure. *Tectonophysics*, 503(1-2):60–74.

Ghanizadeh, A., Gasparik, M., Amann-Hildenbrand, A., Gensterblum, Y., and Krooss, B. M. (2013). Lithological controls on matrix permeability of organic-rich shales: an experimental study. *Energy Procedia*, 40:127–136.

Giggenbach, W. F. (1995). Variations in the Chemical and Isotopic Composition of Fluids Discharged from the Taupo Volcanic Zone, New-Zealand. *J. Volcanol. Geotherm. Res.*, 68(95):89–116.

Grant, M. A. and Bixley, P. F. (2011). *Geothermal Reservoir Engineering*. USA (2nd Edition), Elsevier, Burlington.

Gravley, D. M., Wilson, C. J. N., and Leonard, G. S. (2007). Double trouble: paired ignimbrite eruptions and collateral subsidence in the Taupo Volcanic Zone, New Zealand. *Geological Society of America Bulletin*, 119(1-2):18–30.

Guéguen, Y. and Palciauskas, V. (1994). *Introduction to the Physics of Rocks*. Princeton University Press USA, Princeton.

Heap, M. J., Baud, P., Meredith, P. G., Vinciguerra, S., and Reuschlé, T. (2014a). The permeability and elastic moduli of tuff from Campi Flegrei, Italy: Implications for ground deformation modelling. *Solid Earth*, 5(1):25–44.

Heap, M. J., Lavallée, Y., Petrakova, L., Baud, P., Reuschlé, T., Varley, N. R., and Dingwell, D. B. (2014b). Microstructural controls on the physical and mechanical properties of edifice-forming andesites at Volcán de Colima, Mexico. *Journal of Geophysical Research: Solid Earth*, 119(4):2925–2963.

Hochstein, M. (1995). Crustal heat transfer in the Taupo Volcanic Zone (New Zealand): comparison with other volcanic arcs and explanatory heat source models. *Journal of Volcanology and Geothermal Research*, 68:117–151.

Hole, H. M. (2013). Geothermal Drilling - Keep it simple. In *35th New Zealand Geothermal Workshop: 2013 Proceedings*, pages 17–20, Rotorua.

Horie, T. and Muto, T. (2010). The world's largest single cylinder geothermal power generation unit - Nga Awa Purua Geothermal Power Station, New Zealand. *Transactions - Geothermal Resources Council*, 34:1039–1044.

Houghton, B. F., Wilson, C. J. N., McWilliams, M. O., Lanphere, M. A., Weaver, S. D., Briggs, R. M., and Pringle, M. S. (1995). Chronology and dynamics of a large silicic magmatic system: Central Taupo Volcanic Zone, New Zealand. *Geology*, 23(1):13.

Hudson, R. and Ulusay, J. A. (2007). *The ISRM Suggested Methods for Rock Characterization, Testing and Monitoring: 2007-2014*. Springer International Publishing Switzerland.

Keshavarz, M., Pellet, F. L., and Loret, B. (2010). Damage and changes in mechanical properties of a gabbro thermally loaded up to 1,000C. *Pure and Applied Geophysics*, 167(12):1511–1523.

Klinkenberg, L. J. (1941). The permeability of porous media to liquids and gases. *API Drilling and Production Practice*, 1:200–213.

Krupp, R. E. and Seward, T. M. (1987). The Rotokawa geothermal system, New Zealand: an active epithermal gold-depositing environment. *Economic Geology*, 82:1109–1129.

Lind, L., Morczek, S., and Bell, J. (2015). Energy Efficient - Rotokawa Geothermal Power Station. *Earth Energy: Accessible; Reliable; Renewable.*

McCutcheon, S. C., Martin, J. L., and Barnwell, T. O. J. (1993). *Handbook of Hydrology.* McGraw-Hill, New York, USA.

McLoughlin, K., Campbell, A., and Ussher, G. (2010). The Nga Awa Purua geothermal project, Rotokawa, New Zealand. In *Proceedings World Geothermal Congress 2010, Bali, Indonesia*, Bali.

McNamara, D. D., Sewell, S., Buscarlet, E., and Wallis, I. C. (2015). A review of the Rotokawa Geothermal Field , New Zealand. *Geothermics*, page http://dx.doi.org/10.1016/j.geothermics.2015.07.00.

Milicich, S. D., Rosenberg, M. D., and Bignall, G. (2008). Geology of Injection Well RK20 , Rotokawa Geothermal Field. Technical Report February, GNS Science, Lower Hutt, New Zealand.

O'Brien, J. M. (2010). Hydrogeochemical Characteristics of the Ngatamariki Geothermal Field and a Comparison with the Orakei Korako Thermal Area, Taupo Volcanic Zone, New Zealand. *Unpublished MSc thesis, University of Canterbury, Christchurch, New Zealand, 156p.*

Palmer, A. S. (1982). Kawakawa Tephra in Wairarapa, New Zealand, and its use for correlating Ohakea loess. *New Zealand Journal of Geology and Geophysics*, 25:305–315.

Quinao, J. J. and Azwar, L. (2012). Correlation of reservoir monitoring and continuous production data to interpret unexpected well behaviour in Rotokawa. In *Proceedings 34th New Zealand Geothermal Workshop*, Auckland, New Zealand.

Rae, A. (2007). Rotokawa Geology and Geophysics. *GNS Science consultancy report 2007/83.*

Rae, A. J., McCoy-West, A., and Ramirez, L. E. (2009). Geology of Production Wells RK26 and RK27, Rotokawa Geothermal Field. *GNS Science Consultancy Report 2009/10*, page 73.

Rae, A. J., McCoy-West, A., Ramirez, L. E., and McNamara, D. (2010). Geology of Production Wells RK30L1 and RK30L2 Rotokawa Geothermal Field. *GNS Science Consultancy Report 2010/02*, page 41.

Ramirez, L. E. and Rae, A. J. (2009). Geology of Injection Well RK24 / RK24ST1 Rotokawa Geothermal Field. *GNS Science Consultancy Report 2009/04*, page 29.

Read, S. A. L., Barker, P. R., and Reyes, A. G. (2001). Consolidation properties of Huka Falls formations - linkages to subsidence at Ohaaki and Wairakei. *Proceedings 23rd NZ Geothermal Workshop.*

Risk, G. F. (2000). Electrical resistivity of the Rotokawa Geothermal Field, New Zealand. *In: Proceedings, 22nd New Zealand Geothermal Workshop.*

Roegiers, J.-C. (1995). Recent rock mechanics developments in the petroleum industry. In *35th U.S. Symposium on Rock Mechanics*, pages 17–29, Reno, Nevada.

Rowland, J. V. and Sibson, R. H. (2001). Extensional fault kinematics within the Taupo Volcanic Zone, New Zealand, Soft linked segmentation of a continental rift system. *New Zealand Journal of Geology and Geophysics*, 44(2):271–283.

Sanders, F., Simpson, M. P., and Chambefort, I. (2015). Geology of Well RK34 and RK34-ST1, Rotokawa Geothermal Field. *GNS Science Consultancy Report 2015/03*.

Sewell, S. M., Cumming, W. B., Aswar, L., and Bardsley, C. (2012). Integrated MT and natural state temperature interpretation for a conceptual model supporting reservoir numerical modelling and well targeting at the Rotokawa Geothermal Field. In *Proceedings Thirty-seventh Workshop on Geothermal Reservoir Engineering, Stanford Univeristy*, Stanford, California.

Siratovich, P. A. (2014). Thermal Stimulation of the Rotokawa Andesite: A Laboratory Approach. *Unpublished PhD thesis, University of Canterbury, Christchurch, New Zealand*.

Siratovich, P. A., Heap, M. J., Villenueve, M. C., Cole, J. W., and Reuschlé, T. (2014). Physical property relationships of the Rotokawa Andesite, a significant geothermal reservoir rock in the Taupo Volcanic Zone, New Zealand. *Geothermal Energy*, 2:10.

Stimac, J. A., Powell, T. S., and Golla, G. U. (2004). Porosity and permeability of the Tiwi geothermal field, Philippines, based on continuous and spot core measurements. *Geothermics*, 33(1-2):87–107.

Vinciguerra, S., Trovato, C., Meredith, P. G., and Benson, P. M. (2005). Relating seismic velocities, thermal cracking and permeability in Mt. Etna and Iceland basalts. *International Journal of Rock Mechanics and Mining Sciences*, 42:900–910.

Vucetich, C. G. and Howorth, R. (1976). Proposed definition of the Kawakawa Tephra, the c. 20,000-years B.P. marker horizon in the New Zealand region. *New Zealand Journal of Geology and Geophysics*, 19(1):43–50.

Vutukuri, V. S. and Lama, R. D. (1940). *Handbook on mechanical properties of rocks : testing techniques and results*. Clausthal, Bay Village, Ohio, USA.

Wallace, L. M. (2004). Subduction zone coupling and tectonic block rotations in the North Island, New Zealand. *Journal of Geophysical Research*, 109(B12):B12406.

Wallis, I. C., Bardsley, C. J., Powell, T. S., Rowland, J. V., and O'Brien, J. M. (2013). A structural model for the Rotokawa Geothermal Field, New Zealand. In *35th New Zealand Geothermal Workshop: 2013 Proceedings*, Rotorua.

Wilson, C. J. N., Houghton, B. F., McWilliams, M. O., Lanphere, M. A., Weaver, S. D., and Briggs, R. M. (1995). Volcanic and structural evolution of Taupo Volcanic Zone, New Zealand: a review. *Journal of Volcanology and Geothermal Research*, 68:1–28.

Winick, J., Powell, T., and Mroczek, E. (2011). The natural-state geochemistry of the Rotokawa reservoir. In *New Zealand Geothermal Workshop 2011 Proceedings*, Auckland, New Zealand.

Wohletz, K. and Heiken, G. (1992). *Volcanology and Geothermal Energy*. University of California Press, Los Angeles.

Wood, M. D. and Rosenberg, C. P. (1997). Geology of production well RK9 and reinjection well RK12: Rotokawa Geothermal Field. *GNS Science Consultancy Report 1997*, page 21.

Wyering, L. D., Villeneuve, M. C., Wallis, I. C., Siratovich, P. A., Kennedy, B. M., Gravley, D. M., and Cant, J. L. (2014). Mechanical and physical properties of hydrothermally altered rocks, Taupo Volcanic Zone, New Zealand. *Journal of Volcanology and Geothermal Research*, 288:76–93.